

1

2 **The ScaLIing Macroweather Model (SLIMM): using**
3 **scaling to forecast global scale macroweather from**
4 **months to decades**

5

S. Lovejoy, L. del Rio Amador, R. Hébert

6

Physics, McGill University,

7

3600 University st., Montreal, Que. H3A 2T8,

8

Canada

9 **Abstract**

10 At scales of ≈ 10 days (the lifetime of planetary scale structures), there is a drastic
11 transition from high frequency weather to low frequency macroweather. This scale is
12 close to the predictability limits of deterministic atmospheric models; so that in GCM
13 macroweather forecasts, the weather is a high frequency noise. But neither the GCM
14 noise nor the GCM climate is fully realistic. In this paper we show how simple stochastic
15 models can be developed that use empirical data to force the statistics and climate to be
16 realistic so that even a two parameter model can perform as well as GCM's for annual
17 global temperature forecasts.

18 The key is to exploit the scaling of the dynamics and the large stochastic memories
19 that we quantify. Since macroweather temporal (but not spatial) intermittency is low, we
20 propose using the simplest model based on fractional Gaussian noise (fGn): the ScaLIing

21 Macroweather Model (SLIMM). SLIMM is based on a stochastic ordinary differential
22 equations, differing from usual linear stochastic models (such as the Linear Inverse
23 Modelling, LIM) in that it is of fractional rather than integer order. Whereas LIM
24 implicitly assumes there is no low frequency memory, SLIMM has a huge memory that
25 can be exploited. Although the basic mathematical forecast problem for fGn has been
26 solved, we approach the problem in an original manner notably using the method of
27 innovations to obtain simpler results on forecast skill and on the size of the effective
28 system memory.

29 A key to successful stochastic forecasts of natural macroweather variability is to
30 first remove the low frequency anthropogenic component. A previous attempt to use fGn
31 for forecasts had disappointing results because this was not done. We validate our
32 theory using hindcasts of global and northern hemisphere temperatures at monthly and
33 annual resolutions. Several nondimensional measures of forecast skill – with no
34 adjustable parameters - show excellent agreement with hindcasts and these show some
35 skill even at decadal scales. We also compare our forecast errors with those of several
36 GCM experiments (with and without initialization), and with other stochastic forecasts
37 showing that even this simplest two parameter SLIMM model is somewhat superior. In
38 future, using a space-time (regionalized) generalization of SLIMM we expect to be able
39 to exploit the system memory more extensively and obtain even more realistic forecasts.

40

41 **1 Introduction**

42 Due to their sensitive dependence on initial conditions, the classical deterministic
43 prediction limit of GCM's is about ten days - the lifetime of planetary sized structures
44 (τ_w). Beyond this, the forecast weather rapidly loses any relationship with the real
45 weather. The analogous scale (τ_{ow}) for near surface ocean gyres is about 1 year
46 ([*Lovejoy and Schertzer, 2012b*]), so that even the ocean component - important in
47 fully coupled climate models (referred to simply as GCM's below) - is poorly forecast
48 beyond this. When using long GCM runs for making climate forecasts, we are therefore
49 really considering a boundary value problem rather than an initial value problem
50 ([*Bryson, 1997*]).

51 For these longer scales, following [*Hasselmann, 1976*], the high frequency
52 weather can be considered as a noise driving an effectively stochastic low frequency
53 system; the separation of scales needed to justify such modelling is provided by the
54 drastic transitions at τ_w , τ_{ow} . In the atmosphere, the basic phenomenology behind this
55 has been known since the earliest atmospheric spectra [*Panofsky and Van der Hoven,*
56 *1955*] and was variously theorized as the "scale of migratory pressure systems of
57 synoptic weather map scale" ([*Van der Hoven, 1957*]) and later as the "synoptic
58 maximum" ([*Kolesnikov and Monin, 1965*]). Later, it was argued to be a transition scale
59 of the order of the lifetime of planetary structures that separated different high frequency
60 and low frequency scaling regimes ([*Lovejoy and Schertzer, 1986*]). More recently,
61 based on the solar-induced energy rate density, the atmospheric scale τ_w was deduced
62 theoretically from turbulence theory [*Lovejoy and Schertzer, 2010*], and τ_{ow} was

63 derived in [Lovejoy and Schertzer, 2013] (ch. 8). The same basic picture was also
 64 confirmed in the Martian atmosphere in [Lovejoy *et al.*, 2014] including a correct
 65 prediction of the low and high frequency spectral exponents and Martian transition scale
 66 τ_{Mw} (=1.8 sols). Although it is only plausible at midlatitudes the competing theory from
 67 dynamical meteorology postulates that the transition scale τ_w is the typical scale of
 68 baroclinic instabilities ([Vallis, 2010]; see the critique in [Lovejoy and Schertzer,
 69 2013], ch. 8).

70 Independent of its origin, the transition justifies the idea that the weather is
 71 essentially a high frequency noise driving a lower frequency climate system and the idea
 72 is exploited in GCM's with long integrations as well as in Hasselmann-type stochastic
 73 modelling, now often referred to as "Linear Inverse Modelling" (LIM; sometimes also
 74 called the "Stochastic Linear Forcing" paradigm), e.g. [Penland and Sardeshmukh,
 75 1995], [Newman *et al.*, 2003], [Sardeshmukh and Sura, 2009]; analogous
 76 modelling is also possible at much longer time scales using energy balance models. For
 77 a review, see [Dijkstra, 2013]; for a somewhat different Hasselmann inspired approach,
 78 see [Livina *et al.*, 2013].

79 In these phenomenological models, the system is regarded as a multivariate
 80 Ornstein-Uhlenbeck (OU) process. The basic LIM paradigm is based on the stochastic
 81 differential equation:

$$82 \quad \left(\frac{d}{dt} + \omega_w \right) T = \sigma_\gamma \gamma(t) \quad (1)$$

83 where T is the temperature, $\omega_w = \tau_w^{-1}$ is the “weather frequency”, σ_γ is the amplitude of
 84 the forcing and $\gamma(t)$ is “ δ correlated” Gaussian white noise forcing with:

$$85 \quad \langle \gamma(t)\gamma(s) \rangle = \delta(t-s); \quad \langle \gamma(t) \rangle = 0 \quad (2)$$

86 “ $\langle \cdot \rangle$ ” indicates ensemble averaging and $\delta(t-s)$ is the Dirac function, t and s are two
 87 different times. This uses the convenient physics notation for the generalized function
 88 $\gamma(t)$; alternatively one may take, $\gamma(t)dt = dW$ where W is a Wiener process.

89 Fourier transforming eq.1 and using the rule $FT.\left[\frac{d^n f}{dt^n}\right] = (i\omega)^n FT.[f]$ where “F.T.”
 90 indicates “Fourier Transform”, the temperature spectrum is thus:

$$91 \quad E_T(\omega) = \langle |\tilde{T}(\omega)|^2 \rangle \approx \frac{\sigma_\gamma^2}{\omega^2 + \omega_w^2} \quad (3)$$

92 where ω is the frequency, the tilde indicates Fourier transform, and at respectively low
 93 and high frequencies, $E_T(\omega) \approx \omega^{-\beta}$ with $\beta_l = 0$, $\beta_h = 2$. A spatial LIM model (for
 94 regional forecasting) is obtained by considering a vector each of whose components is the
 95 temperature (or other atmospheric field) at different (spatially distributed) “pixels”,
 96 yielding a system of linear stochastic ordinary differential equations of integer order. A
 97 system with 20 degrees of freedom (involving >100 empirical parameters) currently
 98 somewhat outperforms GCM’s for global scale annual temperature forecasts ([Newman,
 99 2013], table 2, fig. 2).

100 The basic problem with the LIM approach, is that although we are interested in the
101 low frequency behaviour, for LIM models it is simply white noise and this has no
102 memory (put $d/dt=0$ in eq. 1); by hypothesis LIM models therefore assume *a priori* there
103 is no long term predictability. However, ever since [*Lovejoy and Schertzer, 1986*],
104 there has been a growing literature ([*Koscielny-Bunde et al., 1998*], [*Huybers and*
105 *Curry, 2006*], [*Blender et al., 2006*], [*Franzke, 2012*], [*Rypdal et al., 2013*], [*Yuan*
106 *et al., 2014*] and see the extensive review in [*Lovejoy and Schertzer, 2013*]) showing
107 that the temperature (and other atmospheric fields) are scaling at low frequencies, with
108 spectra significantly different than those of Orenstein- Uhlenbeck processes, notably with
109 β_l in the range 0.2 - 0.8 with the corresponding low frequency weather regime (at scales
110 longer than $\tau_w \approx 10$ days) now being referred to as “macroweather” [*Lovejoy, 2013*]. At
111 a theoretical level, for regional forecasting, a further shortcoming of the LIM approach is
112 that it doesn’t respect the property of space-time statistical factorization [*Lovejoy and*
113 *Schertzer, 2013*], ch. 10, [*Lovejoy and de Lima, 2015*].

114 While the difference in the value of β_l might not seem significant, the LIM white
115 noise value $\beta_l = 0$, has no low frequency predictability whereas the actual values $0.2 < \beta_l$
116 < 0.8 (depending mostly on the land or ocean location) correspond to potentially
117 enormous predictability (see e.g. fig. 1a-e). Although this basic feature of “long range
118 statistical dependency” has been regularly pointed out in the scaling literature and an
119 attempt was already made to exploit it ([*Baillie and Chung, 2002b*]; see below), the
120 actual extent of this enhanced predictability has not been quantified before now (see
121 however [*Yuan et al., 2014*]), it justifies the development of the new “ScaLIng

122 Macroweather Model” (SLIMM) that we present below. We argue that even in its
123 simplest two parameter version, that it already is comparable to - or better - than GCM’s.

124

125 **2 Stochastic models and fractional Gaussian noise**

126 **2.1 Linear and nonlinear stochastic atmospheric models**

127 We have discussed the phenomenological linear stochastic models introduced in
128 atmospheric science by Hasselmann and others from 1976 onwards. Yet there is an older
129 tradition of stochastic atmospheric modelling that can be traced back to the 1960’s:
130 stochastic cascade models for turbulent intermittency ([*Novikov and Stewart, 1964*],
131 [*Yaglom, 1966*], [*Mandelbrot, 1974*], [*Schertzer and Lovejoy, 1987*]). Significantly,
132 these models are nonlinear rather than linear and the nonlinearity plays a fundamental
133 role in their ability to realistically model intermittency. By the early 1980’s it was
134 realized that these multiplicative cascades were the generic multifractal processes and
135 they were expected to be generally relevant in high dimensional nonlinear dynamical
136 systems that were scale invariant over some range. By 2010, there was a considerable
137 body of work showing that atmospheric cascades were anisotropic – notably with
138 different scaling in the horizontal and vertical directions (leading to anisotropic, stratified
139 cascades), and that this enabled cascades to operate up to planetary sizes (see the reviews
140 [*Lovejoy and Schertzer, 2010*], [*Lovejoy and Schertzer, 2013*]). While the driving
141 turbulent fluxes were modelled by pure cascades, the observables (temperature, wind
142 etc.) were modelled by fractional integrals of the latter (see below): the Fractionally
143 Integrated Flux (FIF) model. Analysis of in situ (aircraft, dropsonde), remotely sensed

144 data, reanalyses as well as weather forecasting models showed that at least up to 5000
 145 km, the cascade processes were remarkably accurate with statistics (up to second order)
 146 typically showing deviations of less than $\approx \pm 0.5\%$ with respect to the theoretical
 147 predictions (see [*Lovejoy and Schertzer, 2013*], ch. 4 for an empirical review).

148 The success of the cascade model up to planetary scales (L_w) showed that the
 149 horizontal dynamics were dominated by the solar induced energy flux ($\epsilon \approx 10^{-3}$ W/Kg
 150 sometimes called the “energy rate density”) and it implies a break in the space-time
 151 cascades at about $\tau_w = \epsilon^{-1/3} L_w^{2/3} \approx 10$ days discussed above. The logical next question was
 152 therefore: what happens if the model is extended in time and the cascade starts at a outer
 153 time scale much longer than τ_w ? In [*Lovejoy and Schertzer, 2013*] (appendix 10A),
 154 some of the mathematical details of this Extended Fractionally Integrated Flux (EFIF)
 155 model were worked out, and it was shown that at frequencies below τ_w^{-1} there would a
 156 nonintermittent (near) Gaussian, (near) scaling regime with generic exponents β_l in the
 157 observed range.

158 Although this (temporally) extended space-time cascade model well reproduces the
 159 basic space-time weather statistics (for scales $< \tau_w$) and the temporal macroweather
 160 statistics (for scales $> \tau_w$), by itself, it was not able to reproduce the *spatial* macroweather
 161 statistics that characterize climate zones and that were strongly intermittent, so that
 162 another even lower frequency climate process was necessary. [In quantitative terms,
 163 empirically, the basic intermittency parameter C_1 that characterizes the intermittency near
 164 the mean is typically low - around 0.01- 0.02 in time - whereas it is typically high -
 165 around 0.15 – 0.2 in space]. It was proposed that – following the basic mathematical

166 structure of the rest of the model - that the new climate process was also multiplicative in
167 nature. This factorization hypothesis was empirically verified on macroweather
168 temperature and precipitation data ([*Lovejoy and Schertzer, 2013*], ch. 10 and
169 [*Lovejoy and de Lima, 2015*] respectively).

170 To summarize; there are three key empirically observed macroweather
171 characteristics that models should respect: low temporal intermittency, high spatial
172 intermittency and statistical space-time factorization. According to the analysis in
173 [*Lovejoy and de Lima, 2015*], the CEFIF model approximately satisfies these
174 properties but has some disadvantages. A practical difficulty is that it requires the
175 explicit modelling of fine temporal (weather scale) resolution which - much like in
176 GCM's . This is computationally wasteful since for macroweather modelling, it is
177 subsequently averaged out in order to model the lower frequency macroweather. A
178 arguably more significant disadvantage is that CEFIF's theoretical properties – including
179 its predictability – are nontrivial and are largely unknown.

180 SLIMM is an attempt to directly model space-time macroweather while respecting
181 the factorization property and by using the comparatively simple, nonintermittent scaling
182 process – fractional Gaussian noise (fGn) - to reproduce the low intermittency temporal
183 behaviour. In the temporal domain, it is thus based on a linear stochastic model (fGn)
184 with reasonably well understood predictability properties and predictability limits. The
185 strong spatial macroweather variability can be modelled either by using multifractal
186 spatial variability (representing very low frequency climate processes) or alternatively -
187 in the spirit of LIM modelling - it can be modelled as a system of (fractional order)

188 ordinary differential equations. In the former case, developed in [*Lovejoy and de Lima,*
189 2015], it turns out to be sufficient to take the product of a spatially nonlinear
190 (multifractal) stochastic model, with a space-time fGn process. The result is a model that
191 is well defined at arbitrary spatial resolutions and with temporal scaling exponents that
192 are the same at every spatial location (this restriction is somewhat unrealistic). In the
193 latter LIM-like case, one fixes the grid scale (the spatial resolution) and then treats each
194 grid point as a component of an N component system of (fractional) ordinary differential
195 equations. In this version of space-time SLIMM, each grid point can have a different
196 temporal scaling exponent corresponding to a different fractional order of differentiation
197 and the system. Although the result is formally closer to the LIM model (albeit with
198 radically different predictability properties) it has the disadvantage that the model
199 properties are not well defined under changes in spatial resolution - they potentially
200 depend strongly on the grid that is used for the spatial discretization. As a final comment,
201 we note that empirically, it is found that macroweather temperature probability
202 distributions have “fat tails” - so that statistical moments of order ≈ 5 diverge [*Lovejoy*
203 *and Schertzer, 2013*], ch. 5, [*Lovejoy, 2014b; 2015b*], see also [*Lovejoy and*
204 *Schertzer, 1986*]). However for the (low order) statistics (e.g. near the mean and
205 variance - first and second order), the deviations from Gaussianity are small enough that
206 fGn can be used as an approximation.

207 **2.2 From LIM to SLIMM**

208 In this paper, we concentrate on the simplest scalar SLIMM model and we illustrate
209 this by hindcasting global scale temperature series. The key change to the LIM model is

210 thus a modification of the low frequency scaling: rather than $\beta_l=0$ (white noise), the
 211 SLIMM model has $1>\beta_l>0$. This can be effected by a simple extension of eq. 1 to yield
 212 the fractional differential equation:

$$213 \quad \frac{d^{H+1/2}}{dt^{H+1/2}} \left(\omega_w + \frac{d}{dt} \right) T = \sigma_\gamma \gamma(t) \quad (4)$$

214 where $H+1/2$ is a fractional order of differentiation. Using

$$215 \quad FT \left[\frac{d^{H+1/2} f}{dt^{H+1/2}} \right] = (i\omega)^{H+1/2} FT[f] ; \text{ this yields the temperature spectrum:}$$

$$216 \quad E_T(\omega) \approx \omega^{-(2H+1)} \frac{\sigma_\gamma^2}{(\omega^2 + \omega_w^2)} \quad (5)$$

217 hence the low and high frequency SLIMM exponents are: $\beta_l = 2H+1$, $\beta_h = 2H+3$. Note
 218 that for the global temperature series analysed below, we have $\beta_l \approx 0.6$ and $H \approx -0.2$ (see
 219 fig. 4a, b).

220 Alternatively, eq. 4 can be solved in real space directly. First, operate on both sides

221 of the above by $\left(\omega_w + \frac{d}{dt} \right)^{-1}$ to obtain:

$$222 \quad \frac{d^{H+1/2}}{dt^{H+1/2}} T = \gamma_s(t); \quad \gamma_s(t) = \sigma_\gamma \int_{-\infty}^t e^{-\omega_w(t-t')} \gamma(t') dt' \quad (6)$$

223 Since the autocorrelation of γ_s is:

$$224 \quad \langle \gamma_s(t) \gamma_s(t - \Delta t) \rangle = e^{-\omega_w \Delta t} \sigma_{\gamma_s}^2; \quad \sigma_{\gamma_s}^2 = \frac{\sigma_\gamma^2}{2\omega_w} \quad (7)$$

225 We see that for lags $\Delta t \gg \omega_w^{-1}$ that γ_s is essentially an uncorrelated white noise: γ_s is
 226 simply γ smoothed over time scales shorter than $\tau_w = \omega_w^{-1}$.

227 If we are only interested in frequencies lower than ω_w , we can therefore simply
 228 solve:

$$229 \quad \frac{d^{H+1/2}}{dt^{H+1/2}} T = \sigma_\gamma \gamma_\tau(t) \quad (8)$$

230 The LIM paradigm is recovered as the special case with $H = -1/2$. Although physically,
 231 the weather scales are responsible for the smoothing at τ_w , in practice, we typically have
 232 climate data averaged at even lower resolutions: for example monthly or annually.
 233 Therefore, it is simpler to consider a “pure” process (with pure white noise forcing γ
 234 rather than the smoothed γ_τ), and then introduce the resolution/smoothing simply as an
 235 averaging procedure.

236 Formally, the solution to eq. 8 is obtained by (Riemann-Liouville) fractional
 237 integration of both sides of the equation by order $H+1/2$:

$$238 \quad T(t) = \frac{\sigma_\gamma}{\Gamma(1/2 + H)} \int_{-\infty}^t (t-t')^{-(1/2-H)} \gamma(t') dt'; \quad -1/2 < H < 0 \quad (9)$$

239 (Γ is the gamma function). $T(t)$ is a “fractional Gaussian noise“ process. By inspection,
 240 the statistics are invariant under translations in time: $t \rightarrow t + \Delta t$ so that this process is
 241 stationary. Although basic processes of this type were first introduced by [Kolmogorov,
 242 1940], since [Mandelbrot and Van Ness, 1968], the usual order one integral of eq. 9 has
 243 received most of the mathematical attention: “fractional Brownian motion” (fBm). An

244 interesting mathematical feature of fBm and fGn is that they are not semi-Martingales
 245 and hence the standard stochastic Itô and Stratovitch calculi do not apply (see [*Biagini*
 246 *et al.*, 2008] for a recent mathematical review). In the present case, this is not important
 247 since we only deal with Wiener integrals (i.e. integrals of fGn with respect to
 248 deterministic functions). The FIF model mentioned earlier has the same mathematical
 249 structure: it suffices to replace γ in eq. 9 by a turbulent flux from a multiplicative cascade
 250 model; this overall model has the same fluctuation exponent H but is intermittent with
 251 moments other than first order and potentially has quite different scaling.

252 While below we use simple averaging to obtain small scale convergence of fGn, for
 253 many purposes, the details of the smoothing at resolution τ are unimportant and it can be
 254 useful to define the particularly simple “truncated fGn” process:

$$255 \quad T_{trun}(t) = \frac{\sigma_\gamma}{\Gamma(1/2 + H)} \int_{-\infty}^t (t + \tau - t')^{-(1/2-H)} \gamma(t') dt'; \quad -1/2 < H < 0 \quad (10)$$

256 where the singular kernel is truncated at scale τ . It can be shown that for large enough
 257 lags Δt , the fluctuation and autocorrelation statistics for truncated fGn are the same as for
 258 the averaged fGn, although, when H approaches zero (from below), the convergence of
 259 the former to the latter becomes increasingly slow. In practice, the truncated model is
 260 often a convenient approximation to the slightly more complex averaged fGn process.

261 2.3 Properties of fGn

262 2.3.1 Definition and links to fBm:

263 Fractional Brownian motion has received far more attention than fractional
 264 Gaussian noise and it is possible to deduce the properties of fGn from fBm. However,
 265 since we are exclusively interested in fGn, it is more straightforward to first define fGn
 266 and then – if needed – define fBm from its integral.

267 The canonical fractional Gaussian noise (fGn) process $G_H(t)$ with parameter H , can
 268 be defined as:

$$269 \quad G_H(t) = \frac{c_H}{\Gamma(1/2 + H)} \int_{-\infty}^t (t-t')^{-(1/2-H)} \gamma(t') dt'; \quad -1 < H < 0 \quad (11)$$

270 where c_H is a constant chosen so as to make the expression for the statistics particularly
 271 simple, see below. First, taking ensemble averages of both sides of eq. 11 we find that
 272 the mean vanishes: $\langle G_{H,\tau}(t) \rangle = 0$. Now, take the average of G_H over a resolution τ :

$$273 \quad G_{H,\tau}(t) = \frac{1}{\tau} \int_{t-\tau}^t G_H(t') dt' \quad (12)$$

274 and define the function F_H which will be useful below:

$$275 \quad F_H(\lambda) = \int_0^{\lambda-1} \left((1+u)^{H+1/2} - u^{H+1/2} \right)^2 du; \quad \lambda \geq 1 \quad (13)$$

276 (u is a dummy variable) with the particular value:

$$277 \quad F_H(\infty) = \pi^{-1/2} 2^{-(2H+2)} \Gamma(-1-H) \Gamma(3/2 + H) \quad (14)$$

278 and the asymptotic expression:

$$279 \quad F_H(\lambda) = F_H(\infty) - \frac{(H+1/2)^2}{-2H} \lambda^{2H} + \dots \quad (15)$$

280 If c_H is now chosen such that:

$$281 \quad c_H = \frac{\Gamma(H+3/2)}{\left[F_H(\infty) + \frac{1}{2H+2} \right]^{1/2}} = \left(\frac{\pi}{2 \cos(\pi H) \Gamma(-2H-2)} \right)^{1/2} \quad (16)$$

282 then we have:

$$283 \quad \langle G_{H,\tau}(t)^2 \rangle = \tau^{2H}; \quad -1 < H < 0 \quad (17)$$

284 This shows that a fundamental property is that in the small scale limit ($\tau \rightarrow 0$), the variance
 285 diverges and H is scaling exponent of the root mean square (RMS) value. This singular
 286 small scale behaviour is responsible for the strong power law resolution effects in fGn.
 287 Since in addition $\langle G_{H,\tau}(t) \rangle = 0$, we see that sample functions $G_{H,\tau}(t)$ fluctuate about zero
 288 with successive fluctuations tending to cancel each other out; this is the hallmark of the
 289 macroweather regime.

290 It is more common to treat fBm whose differential $dB_{H'}(t)$ is given by:

$$291 \quad dB_{H'} = G_{H'}(t) dt; \quad H' = H + 1; \quad 0 < H' < 1 \quad (18)$$

292 so that:

$$293 \quad \Delta B_{H'}(\tau) = B_{H'}(t) - B_{H'}(t - \tau) = \int_{t-\tau}^t G_{H'}(t') dt' = \tau G_{H',\tau}(t) \quad (19)$$

294 with the property:

$$295 \quad \langle \Delta B_{H'}(\Delta t)^2 \rangle = \Delta t^{2H'} \quad (20)$$

296 While this defines the increments of $B_{H'}(t)$ and shows that they are stationary, it does not
 297 completely define the process, for this, one conventionally imposes $B_{H'}(0)=0$, leading to
 298 the usual definition due to [*Mandelbrot and Van Ness, 1968*]:

$$299 \quad B_{H'}(t) = \frac{c_{H'}}{\Gamma(H'+1/2)} \int_{-\infty}^0 \left((t-s)^{H'-1/2} - (-s)^{H'-1/2} \right) \gamma(s) ds + \frac{c_{H'}}{\Gamma(H'+1/2)} \int_0^t (t-s)^{H'-1/2} \gamma(s) ds$$

300 (21)

301 Whereas fGn has a small scale divergence that can be eliminated by averaging over a
 302 finite resolution τ , the fGn integral $\int_{-\infty}^t G_H(t') dt'$ on the contrary has a low frequency
 303 divergence. This is the reason for the introduction of the second term in the first integral
 304 in eq. 21: it eliminates this divergence at the price of imposing $B_{H'}(0) = 0$ so that fBm is
 305 nonstationary (although its increments are stationary, eq. 19).

306 A comment on the parameter H is now in order. In treatments of fBm, it is usual to
 307 use the parameter H confined to the unit interval i.e. to characterize the scaling of the
 308 increments of fBm. However, fBm (and fGn) are very special scaling processes, and
 309 even in low intermittency regimes such as macroweather – they are at best approximate
 310 models of reality. Therefore, it is better to define H more generally as the fluctuation
 311 exponent (see below); with this definition H is also useful for more general (multifractal)
 312 scaling processes although the interpretation of H as the ‘‘Hurst exponent’’ is only valid
 313 for fBm). When $-1 < H < 0$, the mean at resolution τ (eq. 12) defines the anomaly

314 fluctuation (see below), so that H is equal to the fluctuation exponent for fGn, in contrast,
 315 for processes with $0 < H < 1$, the fluctuations scale as the mean differences and eq. 20
 316 shows that H' is the fluctuation exponent for fBm. In other words, as long as an
 317 appropriate definition of fluctuation is used, H and $H' = 1 + H$ are fluctuation exponents of
 318 fGn, fBm respectively. The relation $H' = H + 1$ follows because fBm is an integral order 1
 319 of fGn. Therefore, since the macroweather fields of interest have fluctuations with mean
 320 scaling exponent $-1/2 < H < 0$, we use H for the fGn exponent and $1/2 < H' < 1$ for the
 321 corresponding integrated fBm process.

322 Some useful relations are:

$$323 \quad \langle dB_{H'}(t)dB_{H'}(s) \rangle = \langle G_H(t)G_H(s) \rangle dsdt = |t-s|^{2H} dsdt \quad (22)$$

324 and:

$$325 \quad \langle (B_{H'}(t_2) - B_{H'}(t_1))(B_{H'}(t_4) - B_{H'}(t_3)) \rangle = \frac{1}{2} \left((t_4 - t_1)^{2H'} + (t_3 - t_2)^{2H'} - (t_3 - t_1)^{2H'} - (t_4 - t_2)^{2H'} \right)$$

326

$$327 \quad (23)$$

328 valid for $0 < H' < 1$ and $t_1 < t_2 \leq t_3 < t_4$ (e.g. [*Gripenberg and Norros, 1996*]).

329 The relationship eq. 23 can be used to obtain several useful relations for finite
 330 resolution fGn. For example:

$$331 \quad \langle G_{H,\tau_1}(t)G_{H,\tau_2}(t-\Delta t) \rangle = \frac{1}{2\tau_1\tau_2} \left((\Delta t + \tau_2)^{2H+2} + (\Delta t - \tau_1)^{2H+2} - \Delta t^{2H+2} - (\Delta t + \tau_2 - \tau_1)^{2H+2} \right); \quad \begin{array}{l} \Delta t \geq \tau \\ -1 < H < 0 \end{array}$$

332

$$333 \quad (24)$$

334 A convenient expression for the special case at fixed resolution $\tau = \tau_1 = \tau_2$ is:

$$R_{H,\tau}(\Delta t) = \langle G_{H,\tau}(t)G_{H,\tau}(t - \Delta t) \rangle = \frac{\tau^{2H}}{2} [(\lambda + 1)^{2H+2} + (\lambda - 1)^{2H+2} - 2\lambda^{2H+2}]; \quad \begin{array}{l} \lambda = \frac{\Delta t}{\tau} \\ \lambda \geq 1 \end{array} \quad (25)$$

335
336
337 $(-1 < H < 0)$. Where $\lambda = \Delta t / \tau$ is the nondimensional lag i.e. measured in integer resolution
338 units. This is convenient since real data is discretized in time and this shows that as long
339 as we correct for the overall resolution factor (τ^{2H}), that the autocorrelation only depends
340 on the nondimensional lag.

341

Since $H < 0$ the large Δt limit is:

$$342 \quad R_{H,\tau}(\Delta t) \approx (H + 1)(2H + 1)\Delta t^{2H}; \quad \Delta t \gg \tau; \quad -1 < H < 0 \quad (26)$$

343 the autocorrelation falls off algebraically with exponent $2H$.

344 2.3.2 Spectrum and Fluctuations

345 Since fGn is stationary, its spectrum is given by the Fourier transform of the
346 autocorrelation function. The autocorrelation is symmetric: $R_{H,\tau}(\Delta t) = R_{H,\tau}(-\Delta t)$, so that
347 for the Fourier Transform we use the absolute value of Δt . Also, we must take the limit
348 of the autocorrelation of small resolution which is the same as using the large λ formula
349 (eq. 26). In this case we obtain:

$$350 \quad E(\omega) = \frac{\Gamma(3 + 2H) \sin \pi H}{\sqrt{2\pi}} |\omega|^{-\beta}; \quad \beta = 1 + 2H \quad (27)$$

351 The relation between β and H is the standard monofractal one, it is valid as long as
 352 intermittency effects are negligible i.e. if we ignore the multifractal “corrections”.
 353 However, sometimes - as here for high order statistical moments - or in the case of
 354 precipitation even for low order moments - these can give the dominant contribution to
 355 the scaling.

356 The spectrum is one way of characterizing the variability as a function of scale
 357 (frequency), however it is often important to have real space characterizations. These are
 358 useful not only for understanding the effects of changing resolution, but also at a given
 359 time scale Δt for studying the full range of variability (i.e. statistical moments other than
 360 second order, probability distributions, etc.). Wavelets provide a general framework for
 361 defining fluctuations, we now give some simple and useful special cases.

362

363 2.3.2.1 *Anomalies:*

364 An anomaly is the average deviation from the long term average and since
 365 $\langle G_H \rangle = 0$, the anomaly fluctuation over interval Δt is simply G_H at resolution Δt rather
 366 than τ :

$$367 \quad (\Delta G_{H,\tau}(\Delta t))_{anom} = \frac{1}{\Delta t} \int_{t-\Delta t}^t G_H(t') dt' = \frac{1}{\Delta t} \int_{t-\Delta t}^t G_{H,\tau}(t') dt' = G_{H,\Delta t}(t) \quad (28)$$

368 Hence using eq. 25:

$$369 \quad \left\langle (\Delta G_{H,\tau}(\Delta t))_{anom}^2 \right\rangle = \Delta t^{2H} \quad (29)$$

370 While this definition of fluctuation is fine for fGn, it is not appropriate for processes with
 371 $H > 0$ since these “wander”, they do not tend to return to any long term value. Anomaly
 372 fluctuations were referred to with the less intuitive term “tendency” fluctuation in
 373 [*Lovejoy and Schertzer, 2012a*].

374

375 *2.3.2.2 Differences:*

376 The classical fluctuation is the difference (the “poor man’s wavelet”):

$$377 \quad (\Delta G_{H,\tau}(\Delta t))_{diff} = G_{H,\tau}(t) - G_{H,\tau}(t - \Delta t) \quad (30)$$

378 Hence:

$$379 \quad \left\langle (\Delta G_{H,\tau}(\Delta t))_{diff}^2 \right\rangle = 2\tau^{2H} \left(1 + \lambda^{2H+2} - \frac{1}{2} \left((\lambda+1)^{2H+2} + (\lambda-1)^{2H+2} \right) \right); \quad \lambda = \frac{\Delta t}{\tau} \quad (31)$$

380 In the large Δt limit we have:

$$381 \quad \left\langle (\Delta G_{H,\tau}(\Delta t))_{diff}^2 \right\rangle \approx 2\tau^{2H} (1 - (H+1)(2H+1)\lambda^{2H}); \quad \lambda = \frac{\Delta t}{\tau} \gg 1 \quad (32)$$

382 Since $H < 0$, the differences asymptote to the value $2\tau^{2H}$ (double the variance). Notice that

383 since $H < 0$, the differences are not scaling with Δt .

384

385 *2.3.2.3 Haar Fluctuations*

386 As pointed out in [*Lovejoy and Schertzer, 2012a*], the preceding fluctuations

387 only have variances proportional to τ^{2H} over restricted ranges of H , specifically $-1 \leq H \leq 0$

388 (anomalies), $0 \leq H \leq 1$ (differences), a more generally useful fluctuation (used below) is the

389 Haar fluctuation (from the Haar wavelet, [*Haar*, 1910]). These are defined as the
 390 differences between the average of the first and second halves of the interval Δt :

$$391 \quad (\Delta G_{H,\tau}(\Delta t))_{Haar} = \frac{2}{\Delta t} \left[\int_{t-\Delta t/2}^t G_{H,\tau}(t') dt' - \int_{t-\Delta t}^{t-\Delta t/2} G_{H,\tau}(t') dt' \right] \quad (33)$$

392 Using eq. 23, we obtain:

$$393 \quad \left\langle (\Delta G_{H,\tau}(\Delta t))_{Haar}^2 \right\rangle = 4\Delta t^{2H} (2^{-2H} - 1) \quad (34)$$

394 this indeed scales as Δt^{2H} and does not depend on the resolution τ .

395

396 **2.4 Using fGn to model and forecast the temperature**

397 Using the definition (eq. 11) of fGn, we can define the temperature as:

$$398 \quad T(t) = \sigma_T G_H(t) \quad (35)$$

399 (i.e. $\sigma_T = \sigma_\gamma / c_H$). Let us now introduce the integral $S(t)$:

$$400 \quad S(t) = \int_{-\infty}^t T(t') dt' = \frac{1}{\Gamma(H+3/2)} \int_{-\infty}^t (t-t')^{H+1/2} \gamma(t') dt' \quad (36)$$

401 Since T is a fractional integral of order $1/2+H$ with respect to white noise, $S(t)$ is a
 402 fractional integral of order $3/2+H = 1/2+H$. Strictly speaking, the above integral
 403 diverges at $-\infty$, however this is not important since we will always take differences over
 404 finite intervals (equivalent to integrating $T(t)$ over a finite interval) and the differences
 405 will converge.

406 We can therefore define the resolution τ temperature as:

$$407 \quad T_\tau(t) = \sigma_T G_{H,\tau}(t) = \frac{S(t) - S(t - \tau)}{\tau} = \sigma_T \frac{B_{H'}(t) - B_{H'}(t - \tau)}{\tau} \quad (37)$$

408 Notice that because of the divergence of $S(t)$ at $-\infty$, we did not define $S(t) = \sigma_T B_{H'}(t)$

409 however the differences do respect: $S(t) - S(t - \tau) = \sigma_T (B_{H'}(t) - B_{H'}(t - \tau))$.

410 Using eq. 35, the τ resolution temperature variance is thus:

$$411 \quad \langle T_\tau^2 \rangle = \sigma_T^2 \tau^{2H} \quad (38)$$

412 From this and the relation $T_\tau(t) = \sigma_T G_{H,\tau}(t)$, we can trivially obtain the statistics of $T_\tau(t)$

413 from those of $G_{H,\tau}(t)$.

414 2.5 Forecasts

415 Since an fGn process at resolution τ is the average of the increments of an fBm,

416 process, it suffices to forecast fBm. There are four important related problems in the

417 prediction of fBm: a) to find the best forecast using finite past data, b) infinite past data.

418 The cases 1) $0 < H < 1/2$ and 2) $1/2 < H < 1$ (with $H' = 1 + H$) must be considered separately.

419 Since $-1/2 < H < 0$, our problem corresponds to cases 2a, 2b. Yaglom solved problem 1b in

420 1955 ([Yaglom, 1955]), Gripenburg and Norros solved 2a, 2b in 1996 ([Gripenberg

421 and Norros, 1996]) and problem 1a was solved by ([Nuzman and Poor, 2000]).

422 [Hirchoren and Arantes, 1998] used the Gripenburg and Norros results for $1/2 < H < 1$ to

423 numerically test the method adapted to fGn, see also [Hirchoren and D'attellis, 1998].

424 Although the [Gripenberg and Norros, 1996] result conveniently expresses the fBm

425 predictions at time t (the “forecast horizon”) directly in terms of the past series for $t \leq 0$,
 426 the corresponding formulae are not simple.

427 The standard approach that they followed yields nontrivial integral equations
 428 (which they solved) in both the finite and infinite data cases. In what follows, we use a
 429 more straightforward method - the general method of innovations (see e.g. [Papoulis,
 430 1965], ch. 13) - and we obtain relatively simple results for the case with infinite past data
 431 (which is equivalent to the corresponding [Gripenberg and Norros, 1996] result). In a
 432 future publication we improve on this by adapting it to the finite data case. The main
 433 new aspect of the forecasting problem with only finite data is that it turns out that not
 434 only do the most recent values (close to $t = 0$) have strong (singular) weighting, but the
 435 data in the oldest available data also have singular weightings. In the words of
 436 Gripenberg and Norros, this is because they are the “closest witnesses” of the distant past.

437 We now derive the forecast result for resolution τ fGn using innovations assuming
 438 that data is available over the entire past (i.e. from $t = -\infty$ to 0). Recall that the
 439 resolution τ temperature at time t is given by:

$$440 \quad T_\tau(t) = \frac{S(t) - S(t - \tau)}{\tau} = \frac{c_H \sigma_T}{\tau \Gamma(H + 3/2)} \left[\int_{-\infty}^t (t - t')^{H+1/2} \gamma(t') dt' - \int_{-\infty}^{t-\tau} (t - \tau - t')^{H+1/2} \gamma(t') dt' - \right]$$

441 (39)

442 ($t > \tau > 0$). We have used the fact that $S(t)$ is a fractional integral of order $H+3/2$ of γ since
 443 the γ 's are effectively independent random variables, they are called “innovations”. If
 444 $T_\tau(t)$ is known for $t \leq 0$, then the above relation can be inverted to obtain $\gamma(t)$ for $t \leq 0$. If $\gamma(t)$

445 is known for $t \leq 0$, then the minimum square (MS) estimator (circumflex) at time $t \geq \tau$ is
 446 given by:

$$447 \quad \hat{T}_\tau(t) = \frac{\hat{S}(t) - \hat{S}(t - \tau)}{\tau} = \frac{c_H \sigma_T}{\tau \Gamma(H + 3/2)} \left[\int_{-\infty}^0 (t - t')^{H+1/2} \gamma(t') dt' - \int_{-\infty}^0 (t - \tau - t')^{H+1/2} \gamma(t') dt' - \right. \\ 448 \quad \left. \right] \quad (40)$$

449 which depends only on $\gamma(t)$ for $t \leq 0$. That this is indeed the MS estimator follows since
 450 the error E_T in this estimator is orthogonal to the estimator. To see this, note that E_T only
 451 depends on $\gamma(t)$ for $t \geq 0$:

$$452 \quad E_T = T_\tau(t) - \hat{T}_\tau(t) = \frac{c_H \sigma_T}{\tau \Gamma(H + 3/2)} \left[\int_0^t (t - t')^{H+1/2} \gamma(t') dt' - \int_0^{t-\tau} (t - \tau - t')^{H+1/2} \gamma(t') dt' \right] \quad (41)$$

453 Since the range of integration for $\hat{T}_\tau(t)$ in eq. 40 is $t' < 0$ whereas the range for the error

454 E_T (eq. 41) is $t' > 0$, $\hat{T}_\tau(t)$, E_T are clearly orthogonal:

$$455 \quad \langle (T_\tau(t) - \hat{T}_\tau(t)) \gamma(s) \rangle = 0; \quad t \geq 0; \quad s < 0 \quad (42)$$

456 We can use this to obtain:

$$457 \quad \langle E_T(t)^2 \rangle = \langle T_\tau(t)^2 \rangle - \langle T_\tau(t) \hat{T}_\tau(t) \rangle = \langle T_\tau(t)^2 \rangle - \langle \hat{T}_\tau(t)^2 \rangle \quad (43)$$

458 Using the substitution $u = -(t - \tau - t')/\tau$ in the integral eq. 41 and the function $F_H(\lambda)$

459 introduced in eq. 13, and using eq. 16 for c_H , we obtain:

$$460 \quad \langle \hat{T}_\tau(t)^2 \rangle = \sigma_T^2 \tau^{2H} \left[\frac{F_H(\infty) - F_H(\lambda)}{F_H(\infty) + \frac{1}{2H+2}} \right] \quad (44)$$

461 and with $F_H(\infty)$ given in eq. 14.

462 Using eq. 43, 44, the error variance is:

$$463 \quad \langle E_T(t, \tau)^2 \rangle = \langle T_\tau(t)^2 \rangle - \langle \hat{T}_\tau(t)^2 \rangle = \sigma_T^2 \tau^{2H} \left[\frac{F_H(\lambda) + \frac{1}{2H+2}}{F_H(\infty) + \frac{1}{2H+2}} \right] = \sigma_T^2 \tau^{2H} \left[\frac{1 + (2H+2)F_H(\lambda)}{1 + (2H+2)F_H(\infty)} \right] \quad (45)$$

464

465 Hence, the fraction of the variance explained by the forecast, the “skill” (S_k) is:

$$466 \quad S_k(\lambda) = \frac{\langle \hat{T}_\tau(t)^2 \rangle}{\langle T_\tau(t)^2 \rangle} = 1 - \frac{\langle E_T(t)^2 \rangle}{\langle T_\tau(t)^2 \rangle} = \left[\frac{F_H(\infty) - F_H(\lambda)}{F_H(\infty) + \frac{1}{2H+2}} \right]; \quad \lambda = t/\tau; \quad \lambda \geq 1 \quad (46)$$

467 Fig. 1 a shows the theoretical skill as a function of H for different forecast horizons, and
 468 fig. 1b for different forecast horizons as a function H . In fig. 1a, dashed reference lines
 469 indicate the three empirically significant values: land ($H \approx -0.3$), global, ($H \approx -0.2$), ocean
 470 $H \approx -0.1$). In fig. 1b, the estimated global value ($H = -0.20 \pm 0.03$, see below) is indicated in
 471 red.

472 This definition of skill is slightly different from the Root Mean Square Skill Score
 473 (RMSSS) that is sometimes used to evaluate GCM’s (see e.g. [Doblas-Reyes et al.,
 474 2013]). The RMSSS is defined as one minus the ratio of the RMS error of the
 475 ensemble-mean prediction divided by the RMS temperature variation:

$$476 \quad RMSSS = 1 - \frac{\langle (T - \hat{T})^2 \rangle^{1/2}}{\langle T^2 \rangle^{1/2}} \quad (47)$$

477 In our case, the forecast is orthogonal to the prediction so that

478 $\langle (T - \hat{T})^2 \rangle = \langle T^2 \rangle - \langle \hat{T}^2 \rangle$ and we obtain:

$$479 \quad \text{RMSSS} = 1 - (1 - S_k)^{1/2} \approx \frac{1}{2} S_k + \frac{1}{8} S_k^2 + \dots \quad (48)$$

480 This shows that S_k and RMSSS are more or less equivalent skill measures both being
 481 in the range 0 to 1. However, GCM forecasts are generally *not* orthogonal to the data
 482 and for them, the RMSSS can be negative.

483 If the process is scaling over an infinite range in the data, but we only have access
 484 to the innovations over a duration λ_{mem} (in “pixels”) then:

$$485 \quad S_{k, \lambda_{mem}, \infty}(\lambda) = \left[\frac{F_H(\lambda + \lambda_{mem}) - F_H(\lambda)}{F_H(\infty) + \frac{1}{2H + 2}} \right]; \quad \lambda \geq 1 \quad (49)$$

486 To illustrate the potentially huge amount of memory in the climate system (especially in
 487 the ocean), we can (somewhat arbitrarily) define the memory in the system by the λ_{mem}
 488 value such that $S_{k, \lambda_{mem}, \infty}(1) / S_{k, \infty, \infty}(1) = 0.9$, the result is shown in fig. 1c. We see that over
 489 land (using $H = -0.3$), the memory estimated this way typically only goes back 15 pixels
 490 (nondimensional time steps), whereas over the ocean (using $H = -0.1$), it is 600. This
 491 means that the annual temperatures over the ocean typically have information from over
 492 600 years in the past whereas over land, it is only for 15 years. Note that these indicate
 493 the memory associated with 90% of the skill (see fig. 1a) and these skill levels fall off
 494 rapidly as H approaches the white noise value $H = -1/2$. We could also note that this
 495 calculation does *not* imply that we if we only had a short length of ocean data that the

496 forecast would be terrible. This is because the calculation is true for the *innovations* (γ 's)
 497 not the temperatures (T 's) themselves (i.e. the data). Even if we only had 10 years of
 498 ocean temperatures, the past from 10 years ago implicitly contains significant information
 499 from the distant past, and can be exploited (see the numerical experiments in [*Hirchoren*
 500 *and Arantes, 1998*]).

501 In the real world, after the removal of the anthropogenic component (see [*Lovejoy*
 502 *and Schertzer, 2013*] and fig. 4c), the scaling regime has a finite length (estimated as \approx
 503 100 years here), so that the memory in the process is finite. In addition, the monthly and
 504 annual resolution series that we hindcast below used memories of $\lambda = 180, 20$ units
 505 (months, years) respectively. The finite memory is easy to take into account; if the
 506 process memory extends over an interval of λ_{mem} units at resolution τ (i.e. over a time
 507 interval $t = \lambda_{mem}\tau$) it suffices to integrate to λ_{mem} instead of infinity; i.e. to replace infinity
 508 by λ_{mem} in eq. 50:

$$509 \quad S_{k, \lambda_{mem}, \lambda_{mem}}(\lambda) = \left[\frac{F_H(\lambda + \lambda_{mem}) - F_H(\lambda)}{F_H(\lambda + \lambda_{mem}) + \frac{1}{2H + 2}} \right]; \quad \lambda_{mem} \geq \lambda \geq 1 \quad (50)$$

510 In fig. 1d we show that the effect of finite memory increases strongly as H moves closer
 511 to zero, and is non negligible, even for $\lambda_{mem} = 180$, the largest used here (for the monthly
 512 series, when $H = -0.17$, the skill is reduced by 3- 5% up to $\lambda = 60$, see the bottom curves in
 513 fig. 1d.

514 It is instructive to compare the skill obtained with the full memory with that if only
 515 the most recent variable $T_\tau(0)$ is used. The latter can be used either as classical
 516 persistence so that the forecast at time $t = \lambda\tau$ forecast to be equal to the present value (no
 517 change) (i.e. $\hat{T}_\tau(t) = T_\tau(0)$) or as “enhanced” persistence in which $T_\tau(0)$ is used as a
 518 linear estimator of $\hat{T}_\tau(t)$. Since the mean of the process is zero, for a single time step $t =$
 519 τ in the future, this is the same as the minimum square forecast made of an order 1
 520 autoregressive model with nondimensional time step = 1: AR(1). Note however this
 521 equivalence is only for a single time step in the future, for forecasts further in the future;
 522 the AR(1) skill decays exponentially, not in a power law manner.

523 In persistence, $\hat{T}_\tau(t) = T_\tau(0)$, the error in the forecast is simply the difference $E_T(t)$
 524 $= \Delta T_\tau(t) = T_\tau(t) - T_\tau(0)$, the skill is therefore $S_k = 1 - \langle \Delta T_\tau^2 \rangle / \langle T_\tau^2 \rangle$. In “enhanced
 525 persistence”, the value $T_\tau(0)$ is simply considered as an estimator and the minimum
 526 square error linear estimator $\hat{T}_\tau(t)$ is only proportional to $T_\tau(0)$. A standard calculation
 527 (e.g. following [Papoulis, 1965], ch. 13) yields: $\hat{T}_\tau(t) = \left[\langle T_\tau(t) T_\tau(0) \rangle / \langle T_\tau(0)^2 \rangle \right] T_\tau(0)$
 528 so that the term in the square brackets “enhances” the persistence value $T_\tau(0)$. Fig. 1e
 529 compares the skill of the three estimators as functions of H for $\lambda=1$ (i.e. using eq. 25 for
 530 the autocorrelation): $\hat{T}_\tau(\tau) = (2^{2H+1} - 1) T_\tau(0)$. Whereas for $H \approx < -0.1$, classical
 531 persistence is quite poor, we see that the enhanced persistence forecast is much better.

532 3 Forecasting the northern hemisphere and global temperatures

533 3.1 The data and the removal of anthropogenic effects

534 In order to test the method, we chose the NASA GISS northern hemisphere and
 535 global temperature anomaly data sets, both at monthly and at annually averaged
 536 resolutions. A significant issue in the development of such global scale series is the
 537 treatment of the air temperature over the oceans which are estimated from sea surface
 538 temperatures; NASA provides two sets, the Land-Ocean Temperature Index (LOTI) and
 539 Land-Surface Air Temperature Anomalies only (Meteorological Station Data): the dT_s
 540 series. According to the site
 541 (http://data.giss.nasa.gov/gistemp/tabledata_v3/GLB.Ts+dSST.txt), LOTI provides a
 542 more realistic representation of the global mean trends than dT_s ; it slightly underestimates
 543 warming or cooling trends, since the much larger heat capacity of water compared to air
 544 causes a slower and diminished reaction to changes; dT_s on the other hand it
 545 overestimates trends, since it disregards most of the dampening effects of the oceans that
 546 cover about two thirds of the earth's surface. In order to compare the two, we used LOTI
 547 for the annual series and dT_s for the monthly series.

548 The prediction formulae assume that the series has the power law dependencies
 549 indicated above with RMS anomaly or Haar fluctuations following Δt^H (eqs. 34), and
 550 spectra with $\omega^{-\beta}$, with $\beta = (1+2H)$ (eq. 27). However, this scaling only holds over the
 551 macroweather regime, and in the industrial epoch, anthropogenic forcing begins to
 552 dominate the low frequency variability at scales $\tau_c \approx 10-20$ years whereas it occurs at
 553 scales $\tau_c \approx 100$ years in the pre-industrial epoch, see [Lovejoy *et al.*, 2013b] and fig. 4d

554 below. However, [*Lovejoy, 2014b*], [*Lovejoy, 2014a*] showed that if the radiative
 555 forcing due to the observed global annually averaged CO₂ concentrations (ρ_{CO_2}) is used
 556 (proportional to $\log_2 \rho_{CO_2}$), that the “effective climate sensitivity” $\lambda_{2 \times CO_2, eff}$ is quite close
 557 to the more usual “transient“ and “equilibrium“ climate sensitivities estimated by GCM’s
 558 and that the residues had statistics over the scale range 1 to ≈ 125 years that were very
 559 close to pre-industrial multiproxy statistics (see table 1).

560 Therefore as a first step, using the [*Frank et al., 2010*] data (extended to 2013 as
 561 described in [*Lovejoy, 2014a*]), we removed the anthropogenic contribution, using:

$$562 \quad T(t) = T_{anth}(t) + T_{nat}(t) \quad (51)$$

$$563 \quad T_{anth}(t) = \lambda_{2 \times CO_2, eff} \log_2(\rho_{CO_2}(t) / \rho_{CO_2, pre}); \quad \rho_{CO_2, pre} = 277 \text{ ppm} \quad a$$

564 where $\rho_{CO_2, pre}$ is the pre-industrial concentration (=277 ppm), the monthly data are shown
 565 as a function of date (fig. 3a) and CO₂ forcing (fig. 3b) with residues shown in fig. 3c.
 566 The effective sensitivities are shown in table 1a. We could note that if alternatively, the
 567 equivalent CO₂ since 1880 was used (“CO₂eq” as estimated in the IPCC AR5 report), the
 568 sensitivities need only be divided by a factor 1.12, and the residues are essentially
 569 unchanged. This is because of the nearly linear relation between the actual CO₂
 570 concentration and the estimated equivalent concentration (correlation coefficient > 0.993;
 571 see table 3 for the standard deviations of the residues, T_{nat}). By using the observed CO₂
 572 forcing as a linear surrogate for all anthropogenic effects we avoid various uncertain
 573 radiative assumptions needed to estimate CO₂eq especially those concerning the cooling
 574 effects of aerosols which are still unsettled. As explained in [*Lovejoy, 2014b*], since the

575 anthropogenic effects are linked via global economic activity, the observed CO₂ forcing
576 is a plausible linear surrogate for all them.

577 From table 2 we see that the sensitivities do not depend on the exact range over
578 which they are estimated (columns 2-4). As we move to the present (column 4 to column
579 2), the sensitivities stay within the uncertainty range of the earlier estimates with the
580 uncertainties constantly diminishing, consistent with the convergence of the sensitivities
581 as the record lengthens. As a consequence, if we determine T_{anth} using the data only up to
582 1998 or up to 2013, there is very little difference: for the global data at monthly
583 resolution, the difference in the standard deviations (SD's) of T_{nat} estimated with the
584 different sensitivities is 0.005K whereas at annual resolutions, it is 0.0035K (for this
585 period, $\Delta \log_2 p_{CO_2} = 0.05$). These differences are larger than the estimated error in the
586 global scale temperatures (estimated as $\pm 0.03K$ for both – the errors have very little scale
587 dependence, [Lovejoy *et al.*, 2013a] and [Lovejoy, 2015a]). From table 2, we see that
588 there is a $\approx 30\%$ difference between the global and monthly sensitivities due to the change
589 from the LOTI (global) to dTs (monthly) series the sensitivities are virtually independent
590 of whether the data is at one month or one year resolution. We also see that the northern
591 hemisphere has systematically higher sensitivities than the entire globe, this is consistent
592 with the larger land mass in the north and the larger sensitivity of land with respect to the
593 ocean.

594 An obvious criticism of the method of effective climate sensitivities is that
595 anthropogenic forcing primarily warms the oceans and only with some lag, the
596 atmosphere. Systematic cross-correlation analysis in [Lovejoy, 2014b], [Lovejoy,

597 2014a] shows that while the residues are barely affected (see rows 2, 3 in table 2 and
598 [Lovejoy, 2014b] for more on this), the values of the sensitivities are affected (see e.g.
599 column 4 in table 2). We may note that using eq. 51 (no lag), or the same but with a lag
600 are equivalent to assuming a linear climate with Green's function given by a Dirac delta
601 function. This and more sophisticated Green's functions are discussed in a future
602 publication.

603 Finally, we can note that the difference between LOTI and dTs temperature is
604 primarily the sensitivities (table 2); that the remaining differences in the residues is
605 mostly due to their different resolutions. From eq. 39 we see that the ratio of RMS
606 fluctuations in these should be λ^H where λ is the resolution ratio, here 12 months/year.
607 Table 1 shows that the H estimated from the RMS values is indeed close to the H
608 estimated more directly in the next subsection. This shows that the main difference
609 between the LOTI and dTs series is indeed their climate sensitivities.

610 In order to judge how close the residues from the CO₂ forcing (eq. 51) are to the
611 true natural variability, we can make various comparisons (table 3). Starting at the top
612 (row 1), we see that, as shown in [Lovejoy, 2014b], the statistics of the resulting residues
613 are very close to those of pre-industrial multiproxies (see also fig. 4c below). In row 3,
614 we see that we take the residues of the 20 year lagged temperatures, there is virtually no
615 difference (although the sensitivities are significantly higher, see table 2). As further
616 reference, (row 4), we see that it is substantially smaller than the standard deviation of the
617 linearly detrended series (i.e. when the residues are calculated from a linear regression
618 with time rather than the forcing).

619 As further evidence that they provide a good estimate of the true natural variability,
620 in rows 5-10 we also show the annual RMS errors of various GCM global temperature
621 hindcasts. For example, in rows 5-6 we compare hindcasts of CMIP 3 GCM's both with
622 and without annual data initialisation, assimilation (rows 5, 6). Without initialization
623 (row 5), the results are half way between the CO₂ forcing residues (i.e. T_{nat} , row 2) and
624 the standard deviation of the linearly detrended series (row 4), i.e. the forecast is poor
625 even for the anthropogenic part. Unsurprisingly, with annual data initialisation,
626 assimilation (row 6) it is much better, but it is apparently still unable to do better than
627 simply estimating the anthropogenic component. We can deduce this since the resulting
628 RMS errors are virtually identical to the standard deviation of the estimated T_{nat} (row 3).
629 This conclusion is reinforced in row 7 where CMIP 3 GCM's (without data initialization)
630 were analyzed. However, in place of annual data initialization, a complex empirical bias
631 and variance correction scheme was implemented in order to keep the statistics of
632 uninitialized hindcasts close to the data. We see that the resulting RMS error is virtually
633 identical to GCM with data initialization (row 6) as well as the standard deviation of T_{nat}
634 (row 3). They are also very close to other GCM estimates of natural variability. These
635 conclusions are reinforced in the 5 year and 9 year "anomaly" columns. As expected -
636 due to the averaging of the temperature in the definition of the anomalies out to the
637 forecast horizon - the RMS error decreases. However, it is still only barely better than
638 the T_{nat} estimates from the residues.

639 Very similar results are indicated in rows 8-10 for other GCM hindcast
640 experiments, these are shown graphically in fig. 2, which is adapted from a multimodel
641 ENSEMBLES experiment hindcasts discussed in [*Garcia-Serrano and Doblas-Reyes,*

642 2012]. The multimodel mean is consistently close to - but generally a little above - T_{nat}
 643 (bottom horizontal line) while remaining better than the standard deviation of the linearly
 644 detrended temperature (top horizontal line). Also shown in table 1 and fig. 2 are the
 645 results of LIM, SLIMM and other stochastic models, these will be discussed further in
 646 section 4. For now suffice it to indicate that the SLIMM model error is bounded above
 647 by the standard deviation of T_{nat} . By using the long range memory to forecast T_{nat} , it can
 648 only do better. It thus generally improves upon the GCM's and - for two year horizons
 649 and beyond – it is better than the >100 parameter LIM model whose 9 year forecast is
 650 essentially equivalent to a linear detrending.

651 **3.2 Estimating H from the residues**

652 Having estimated T_{nat} by removing the anthropogenic contribution, we may now
 653 test the quality of the scaling and estimate H . Figure 4a shows the raw spectra of the
 654 residues showing the scaling but with large fluctuations (as expected) with $\beta \approx 0.60$. We
 655 have already mentioned that the intermittency is low in this macroweather regime,
 656 indeed using exponents estimated in [*Lovejoy and Schertzer, 2013*], the resulting
 657 multifractal corrections to the variance are $\approx 0.01 - 0.02$ so that we may use the
 658 monofractal relation $\beta = 1 + 2H$ which yields: $H \approx -0.20$. Slightly more accurate estimates
 659 can be obtained by averaging the spectrum over logarithmically spaced bins (fig. 4b, and
 660 by compensating the spectrum by dividing it by the theoretical spectrum with $\beta = 0.54$ (H
 661 $= -0.17$). This figure makes the estimate $\beta = 0.20 \pm 0.06$ ($H = -0.20 \pm 0.03$) plausible.
 662 Finally, the corresponding RMS Haar fluctuations are shown in fig. 4c, we see that they
 663 plausibly follow $H = -0.20$ out to about 100 years (the sharp drop at the largest lag is not

664 significant: it corresponds to a single long fluctuation that is somewhat biased since some
 665 of the low frequency natural variability is also removed when T_{nat} is estimated by the
 666 method of residuals.

667 Also shown for reference in fig. 4c is the GISS-E2-R millennium control run (with
 668 fixed forcings), as well as the RMS fluctuations for three pre-industrial multiproxies.
 669 We see that out to about 100 year scales, all the fluctuations have nearly the same
 670 amplitudes as functions of scale giving supporting the idea that T_{nat} as estimated by
 671 residuals is indeed a good estimate of the natural variability, and also confirming the
 672 estimate the global scale exponent value $H = -0.20 \pm 0.03$.

673 As a final comparison, fig. 4d shows RMS Haar fluctuations for the global
 674 averages (from fig. 4c), land only averages and from the oceans - the Pacific Decadal
 675 Oscillation (PDO). The PDO is the amplitude of the largest eigenvalue of the Pacific Sea
 676 Surface Temperature autocorrelation matrix (i.e. the amplitude of the most important
 677 Empirical Orthogonal Function: EOF). For the land only curve, notice the sharp rise for
 678 scales $\gg 10$ years; this is the effect of the anthropogenic signal that was not removed in
 679 this series. Overall we see that (roughly) for land $H \approx -0.3$, for the globe, $H = -0.2$, and for
 680 the oceans, $H = -0.1$. Fig. 1a, c shows the drastic differences in memory implied by these
 681 apparently small changes in H .

682 **4 Testing SLIMM by hindcasting**

683 **4.1 The numerical approach**

684 The theory for predicting fGn leads to the general equation for the variance of
 685 forecast error (E_T) at forecast horizon t , resolution τ , eq. 45. In order to test the equation

686 on the temperature residues, we can use the global and northern hemisphere series
 687 analyzed in the previous section and systematically make hindcasts. In this first study,
 688 we took a simple, straightforward approach based on the method of innovations. We
 689 discretised eq. 9, which was then written as a matrix equation of the form: $T_t = \sum_{t' < t} M_{t,t'} \gamma_{t'}$
 690 where the indices refer to the discrete time nondimensionalized by the series resolution,
 691 and $M_{t,t'}$ which is the (singular) kernel from the fractional integration. The sum was over
 692 finite past of length $t_{mem} = \lambda_{mem} \tau$ units (see below) and the matrix was then inverted to
 693 yield the corresponding innovations γ_t . To make the forecast at time $t + \Delta t$ (i.e. Δt units in
 694 the future), the equation was used with an augmented kernel $M_{t+\Delta t,t'}$ with the innovation
 695 vector lengthened by appending Δt zeroes (the expectation values of the unknown future
 696 innovations) to the t_{mem} innovations that were determined in the previous step.

697 While our approach has the advantage of being straightforward (and it was tested
 698 on numerical simulations of fGn), in future applications improvements could be made.
 699 For example, by using a Girsanov formula, we could rewrite fGn in terms of a finite
 700 integral (see [*Biagini et al., 2008*]), and the discretised numerics would then be more
 701 accurate (this is especially important for H near the limiting values 0 and $-1/2$).
 702 Alternatively, we could use [*Gripenberg and Norros, 1996*] integral equation approach
 703 discretized with a variant of the [*Hirchoren and Arantes, 1998*], approach which
 704 notably has the advantage of requiring less past data.

705 **4.2 The hindcasts**

706 In order to obtain good hindcast error statistics, it is important to make and validate
 707 as many hindcasts as possible, i.e. one for each discretised time that is available.
 708 However, due to the long-range correlations, we want to use a reasonable number of past
 709 time steps in the hindcast for memory, so that the earliest possible hindcast will be later
 710 than the earliest available data by the corresponding amount. The compromise used here
 711 consisted of dividing the 134 year series into 30 annual blocks (annual resolution) and 20
 712 year blocks (monthly resolution). In each block in the annual series, the first 20 years
 713 were used as “memory” to develop the hindcast over the next 10 years so that for
 714 estimating the hindcast errors: a total of $134-30=104$ forecasts were made. For the
 715 monthly series, the same procedure involved blocks of 240 months: 180 months for the
 716 memory and 60 months for the hindcast for a total of $1608-240=1368$ hindcasts.

717 The hindcasts can be evaluated at various resolutions and forecast horizons, eqs. 46,
 718 49, 50 gives the general theoretical results. The cases of special interest are the
 719 temperature hindcasts and the anomaly hindcasts with (resolutions, horizons) of $(\tau, \lambda\tau)$
 720 and $(\lambda\tau, \lambda\tau)$ respectively. The error variance ratios (R) are:

$$721 \quad R_{temp} = \frac{\langle E_T(\lambda\tau, \tau)^2 \rangle}{\langle E_T(\tau, \tau)^2 \rangle} = 1 + (2 + 2H)F_H(\lambda) \quad (52)$$

722 and:

$$723 \quad R_{anom} = \frac{\langle E_T(\lambda\tau, \lambda\tau)^2 \rangle}{\langle E_T(\tau, \tau)^2 \rangle} = \lambda^{2H} \quad (53)$$

724 Both ratios are shown in fig. 5 along with the exact theory curves and table 3 gives
725 the corresponding highest resolution standard deviations (for both lagged and unlagged
726 estimates of T_{nat} , there is virtually no difference). It is seen that all the forecast error
727 variances (global, northern, annual, monthly resolution) collapse quite well between the
728 theory curves corresponding to $H = -0.17$ and $H = -0.23$ corresponding to $H \approx -0.20 \pm 0.03$
729 (although they are closer to the $H = -0.17$ curves). It is important to stress that fig. 5 is
730 completely nondimensional, it depends on a single parameter (H), and this parameter was
731 estimated earlier using a quite different technique (Haar fluctuations and spectra) that had
732 no direct relation to the property being measured (forecast skill). We have effectively
733 used spectral and Haar and spectral analysis of scaling to determine the accuracy of
734 forecasts using no extra information. Figure 5 has no adjustable parameters so that the
735 agreement of the hindcast errors with theory is a particularly strong confirmation of the
736 theory. We could add that the fact that the errors depend only on the dimensionless
737 forecast horizon is also a consequence of the scaling, i.e. on the lack of strong
738 characteristic time scale in the macroweather regime.

739 Since the anomaly errors are power laws (eq. 54), they can conveniently be evaluated
740 on a log-log plot; see fig. 6. Note that the RMS anomaly errors decrease with forecast
741 horizon. The reason is that while forecasts further and further in the future lose
742 accuracy, this loss is more than compensated by the decrease in the variance due to the
743 lower resolution, so that the anomaly variance decreases. Finally, we could note that the
744 method has been applied to explaining the “pause” or “hiatus” in the global warming
745 since 1998 as well as to make a forecast to 2023 [Lovejoy, 2015b].

746 **4.3 Hindcast Skill**

747 Another way to evaluate the hindcasts is to determine their nondimensional skills
748 i.e. the fraction of the variance that they explain (see the general formula eq. 46). From
749 the formula, we can see that the skill depends only on the nondimensional forecast
750 horizon $\lambda = t/\tau$. Therefore the skill for forecast anomalies – i.e. the average of the
751 forecast up to the horizon i.e. $t = \tau$, hence $\lambda=1$, has the remarkable property of being
752 constant, independent of the horizon. The reason is that while forecasts further and
753 further in the future lose accuracy, this loss is exactly compensated by the decrease in
754 the variance due to the lower resolution, so that the anomaly skill doesn't change. Fig. 7
755 is another example of a nondimensional plot where the theory involves no adjustable
756 parameters, it shows that the theoretical prediction is well respected by the global,
757 northern hemisphere annual and global resolution series. Since we estimated $H =$
758 -0.20 ± 0.03 , it can be seen that the skill for the monthly series is nearly as high as
759 theoretically predicted up to a year or so for the global, but up to several years for the
760 northern hemisphere series. The global series has slightly lower forecast skill than
761 theoretically predicted, but is still of the order of 15% at 10 years. Also shown is the effect
762 of using only a finite part of the memory.

763 The skill in usual temperature forecasts (i.e. with fixed resolution τ , and increasing
764 horizon $t = \lambda\tau$) is shown in fig. 8. We see that monthly series can be predicted to nearly
765 the theoretical limit up to about 2- 3 years ($\approx 5\%$ skill), for the annual series, this is up to
766 about 5 years ($\approx 10\%$ skill). Again the results are close to the $H = -0.17$ theory.

767 **4.4 Hindcast Correlations**

768 A final way to evaluate the hindcasts is to calculate the correlation coefficient
769 between the hindcast and the temperature:

$$770 \quad \rho_{\hat{T}_\tau, T_\tau}(t, \tau) = \frac{\langle \hat{T}_\tau(t) T_\tau(t) \rangle - \langle \hat{T}_\tau(t) \rangle \langle T_\tau(t) \rangle}{\langle \hat{T}_\tau(t)^2 \rangle^{1/2} \langle T_\tau(t)^2 \rangle^{1/2}} \quad (54)$$

771 Since $\langle T \rangle = 0$, the cross term vanishes; using eq. 44 we obtain the simple result:

$$772 \quad \rho_{\hat{T}_\tau, T_\tau}(t, \tau) = \left(\frac{F_H(\infty) - F_H(\lambda)}{F_H(\infty) + \frac{1}{2H+2}} \right)^{1/2}; \quad \lambda = \frac{t}{\tau} \quad (55)$$

773 i.e. $\rho_{\hat{T}_\tau, T_\tau}(t, \tau) = S_k(t, \tau)^{1/2}$ a result which depends on the consequences of orthogonality:

774 $\langle T_\tau(t) \hat{T}_\tau(t) \rangle = \langle \hat{T}_\tau(t)^2 \rangle$ (eq. 42). Asymptotically for $\lambda \gg 1$:

$$775 \quad \rho_{\hat{T}_\tau, T_\tau}(t, \tau) \approx 2^{H+1/2} \left(H + \frac{1}{2} \right) U^{1/2} \lambda^H; \quad \lambda \gg 1; \quad U = \frac{\sqrt{\pi}}{2\Gamma(1-H)\Gamma\left(\frac{3}{2} + H\right)} \quad (56)$$

776 In the special cases of anomalies $t = \tau$, $\lambda = 1$ and we obtain:

$$777 \quad \rho_{\hat{T}_\tau, T_\tau}(t, t) = \sqrt{1 + HU 2^{2H+2}} \quad (57)$$

778 so that the correlations are constant at all forecast horizons. Over the range $-1/2 < H < 0$,
779 the constant U is conveniently close to unity.

780 As in the previous hindcast error analyses, the series were broken into blocks and
781 the forecasts were repeated as often as possible; each forecast was correlated with the

782 observed sequence and averages were performed over all the forecasts and verifying
783 sequences (the mean correlation given by the thick lines), fig. 9. The uncertainty in the
784 hindcast correlation coefficients was estimated by breaking the hindcasts into thirds: three
785 equal sized groups of blocks with the error being given by the standard deviation of the
786 three about the mean (dashed lines). Also shown in fig. 9 are the theoretical curves (eq.
787 54) for $H = -0.20$, in this case the dashed lines indicate the theory for one standard
788 deviations in H i.e. for $H = -0.17, H = -0.23$.

789 As predicted by eq. 57, the anomaly correlations are relatively constant up to about
790 5 years for the annual data (top row), and nearly the same for the monthly data (bottom
791 row). In addition, the northern hemisphere series (blue) are somewhat better forecast
792 than the global series (red). It can be seen that temperature forecasts (i.e. with fixed
793 resolutions) have statistically significant correlations out to 8-9 years for the annual
794 forecasts, out to about 2 years for the monthly global and nearly 5 years for the monthly
795 northern hemisphere forecasts (bottom dashed lines). The anomaly forecasts are
796 statistically significantly correlated at all forecast horizons. Fig. 9 provides more
797 examples of nondimensional plots with no free parameters, and again the agreement with
798 the hindcasts validation is remarkable.

799 Although the results for the anomaly correlations are quite close to those of
800 hindcasts in [*Garcia-Serrano and Doblas-Reyes, 2012*], the latter are for the entire
801 temperature forecast, not just the natural variability as here. This means that the GCM
802 correlations will be augmented with respect to ours due to the existence of long term

803 anthropogenic trends in both the data and the forecasts that are absent in ours (but even
804 with this advantage, their correlations are not higher).

805 **4.5 Comparison with GCM's, LIM, AR(1) and ARFIMA hindcasts**

806 In table 1 and fig. 2, we have already compared GCM hindcast errors with
807 estimates of the natural variability (T_{nat}) from the residues of a linear regression on the
808 CO₂ radiative forcing since 1880. We found that the annual, global GCM hindcasts had
809 errors that were close to, but generally larger than the standard deviation of T_{nat} ($\langle T_{nat}^2 \rangle^{1/2}$)
810 but smaller than the standard deviation of the linearly detrended temperature series (the
811 horizontal lines in fig. 2). $\langle T_{nat}^2 \rangle^{1/2}$ is the RMS error of an unconditional forecast (i.e. with
812 no knowledge of the past): $\langle T_{nat,\tau}^2 \rangle = \langle E_T^2(\tau, \infty) \rangle$ (see eq. 45), it is the upper bound to the
813 hindcast errors. In figure 2, we see that the one-parameter stochastic hindcast (with $H =$
814 -0.2) is somewhat better than the GCM's up to about 6 years after which it is about the
815 same. This bolsters the hypothesis that GCM's primarily model the anthropogenic
816 temperature change, not the natural variability whereas SLIMM has some skill in
817 forecasting the latter.

818 Table 2 and fig. 2 also compare these to LIM hindcasts modelled with 20 degrees of
819 freedom (involving > 100 parameters). We see that LIM is slightly better than SLIMM
820 for horizons up to about 2 years beyond which SLIMM is better. According to the
821 analysis in [Newman, 2013], for periods beyond about a year, the forecasts are mostly
822 determined by the two most important Empirical Orthogonal Functions (EOF's), and
823 their skill decays exponentially, not as a power law. From fig. 2, their main effect seems

824 to be to remove the long term linear trend allowing LIM to have an asymptotic RMS
825 error roughly equal to the standard deviation of the linearly detrended series (the upper
826 horizontal line).

827 Finally, in table 1, rows 12, 13, we have compared the errors with those of an early
828 attempt at scaling temperature forecasts using the AutoRegressive Fractionally Integrated
829 Moving Average process (ARFIMA) [Baillie and Chung, 2002b] along with the
830 corresponding order one AutoRegressive (AR(1)) process. Unfortunately, the forecasts
831 were made by taking 10 year segments and in each removing a separate linear trend so
832 that the low frequencies were not well accounted for (see the footnote to the table for
833 more details). The AR(1) results were not so good: close to the standard deviations of the
834 detrended temperatures. As expected - because it assumes a basic scaling framework - the
835 ARFIMA results were somewhat better. Yet they are substantially worse than the other
836 methods, probably because they did not remove the anthropogenic component first.

837 **5 Conclusions**

838 GCM's are basically weather models whose forecast horizons are well beyond the
839 deterministic predictability limits, corresponding to many lifetimes of planetary scale
840 structures: the macroweather regime. In this regime - that extends from about 10 days to
841 ≈ 100 years (preindustrial), the weather patterns that are generated are essentially random
842 noise. With fixed boundary conditions, GCM's therefore converge asymptotically (in a
843 power law manner, fig. 4c) to their (model) climates. In order to model the low
844 frequency variations associated with the climate proper, the GCM's must be externally
845 forced; if the forcing is strong enough, in principle it can reverse the trend of

846 macroweather fluctuations decreasing with increasing time scale and initiate a new
847 climate regime where fluctuations instead increase with scale (qualitatively similar to
848 their behaviour in the higher frequency weather regime, see [*Lovejoy et al.*, 2013b]). In
849 the real world (pre-industrial), this occurs somewhere around 100 years and fluctuations
850 increasing in scaling manner (but now with $H > 0$) out to ice-age time scales ($\approx 50 - 100$
851 kyrs; note that this 100 year pre-industrial transition scale apparently has large
852 geographical variability, see [*Lovejoy and Schertzer*, 2013], section 11.1.4). At these
853 scales, in addition to solar, and volcanic forcings, the real world may involve new, slow
854 internal processes that become important.

855 In this view, the problem with the GCM approach is that in spite of massive
856 improvements over the last 40 years, the weather noise that they generate isn't totally
857 realistic nor does their climate coincide exactly with the real climate. In an effort to
858 overcome these limitations, stochastic models have been developed that directly and
859 more realistically model the noise and use real world data to exploit the system's memory
860 so as to force the forecasts to be more realistic.

861 The main approaches that could potentially overcome these limitations are the
862 stochastic ones. However, going back to [*Hasselmann*, 1976] these only use integer
863 ordered differential equations, they implicitly assume that the low frequencies are white
864 noises - and hence cannot be forecast with any skill. Modern versions – the Linear
865 Inverse Models (LIM) add sophistication and a large number of (usually, but not
866 necessarily) spatial parameters, but they still impose a short (exponentially correlated)
867 memory and they focus on periods up to a few years at most. This contrasts with

868 turbulence based nonlinear stochastic models which assume that the system is scaling
869 over wide ranges. When they are extended to the macroweather regime (the Extended
870 Fractionally Integrated Flux – EFIF- model), these scaling models have low
871 intermittency, scaling fluctuations with temporal exponents close to those that are
872 observed by a growing macroweather scaling literature. Contrary to their behaviour in
873 the weather regime, in macroweather they are only weakly nonlinear. However,
874 empirically, the spatial macroweather variability is very high so that [*Lovejoy and*
875 *Schertzer, 2013*] already proposed that the EFIF model be spatially modulated by a
876 multifractal climate process (yielding the Climate EFIF model, CEFIF) whose temporal
877 variability was at such low frequencies so as to be essentially constant in time over the
878 macroweather regime.

879 The CEFIF model is complex both numerically and mathematically and it's
880 prediction properties are not known. In this paper, we therefore make a simplified model,
881 the ScaLIing Macroweather Model (SLIMM) that can be strongly variable (intermittent)
882 in space, Gaussian (nonintermittent) in time. The simplest relevant model of the temporal
883 behaviour is thus fractional Gaussian noise (fGn) whose integral is the better known
884 fractional Brownian motion (fBm) process (see [*Lovejoy and de Lima, 2015*] for this
885 regional SLIMM model). A somewhat different way of introducing the spatial variability
886 is to follow the Linear Inverse Modelling (LIM) approach and treat each (spatial) grid
887 point as a component of a system vector. In this case, SLIMM can be obtained as a
888 solution of a fractional order generalization of the usual LIM differential equations.
889 Although in future publications we will show how to make regional SLIMM forecasts, in

890 this paper, we only discuss the scalar version for single time series – here global scale
891 temperatures.

892 In section 2, we situate the process in the mathematical literature and derive basic
893 results for forecasts and forecast skill. These results show that a remarkably high level
894 of skill is available in the climate system; for example for forecast horizons of one
895 nondimensional time unit in the future (i.e. horizons equal to the resolution), the forecast
896 skills – defined as the fraction of the variance explained by the forecast - are 15%, 35%,
897 64% for land, the whole globe and oceans respectively (fig. 1b; taking rough exponent
898 values $H = -0.3, -0.2, -0.1$ respectively, fig. 4c). To quantify the size of the memory, it
899 can be defined as the number of nondimensional units needed to supply 90% of the full
900 memory of the system. Using the same empirical exponents, we found that the memory
901 is 15, 50, 600 for typical land, the globe and typical ocean regions respectively.

902 The SLIMM model forecasts the natural variability. While the responses to solar
903 and volcanic forcings are implicitly included in the forecast, the responses to the
904 anthropogenic forcings are not; we must therefore remove the anthropogenic component
905 which becomes dominant at scales of 10 - 30 years. For this, we follow [Lovejoy,
906 2014b] who showed that the CO₂ radiative forcing is a good linear proxy for all the
907 anthropogenic effects (including the difficult to estimate cooling due to aerosols) so that
908 the natural variability is the residue with respect to a regression against the forcing. In
909 table 1 and in fig. 2, we showed that the resulting standard deviation (± 0.109 K) is very
910 close to the RMS errors in annual, globally averaged GCM temperature hindcasts that use
911 annual data initialisation, assimilation. Indeed, to a good approximation, all the models

912 have errors bounded between this estimate of the natural variability and the slightly
913 higher standard deviation of the linearly detrended temperature series (± 0.163 K). This is
914 true in spite of the fact that they are “optimistic” since they assume that the future
915 volcanic and solar forcings are known in advance. The only partial exception is the
916 stochastic LIM model (with > 100 parameters) which is only marginally better (± 0.085
917 K) than SLIMM for forecast horizons of one to two years after which it asymptotes to the
918 linearly detrended standard deviation.

919 Using the method of innovations, we developed a new way of forecasting fGn that
920 allows SLIMM hindcasts to be made; the long-time forecast horizon RMS error is thus
921 ± 0.109 K, the exploitation of the memory with the single parameter – the exponent $H \approx$
922 0.20 ± 0.03 - reduces this to $\approx \pm 0.093$ K for one year global hindcasts so that SLIMM
923 remains better than or comparable to the multimodel GCM mean (fig. 2).

924 This paper only deals with single time series (global scale temperatures) but it is
925 nevertheless ideal for revisiting the problem of the “pause” or “slow down”, “hiatus” in
926 the warming since 1998 which is a global scale phenomenon. [*Lovejoy, 2015b*] shows
927 how SLIMM hindcasts nearly perfectly predict this hiatus. However, most applications
928 involve predicting the natural variability at regional scales. A future publication shows
929 how this can be done and quantifies the improvement that the additional information
930 (from the regional memory) makes to the forecasts. For forecasts from months to a
931 decade or so, the SLIMM forecast are potentially better than alternatives.

932

933 **6 Acknowledgements**

934 We thank C. Penland and P. Sardeshmukh for helpful discussions. There are no
 935 conflicts of interest, this work was unfunded although L. del Rio Amador thanks
 936 HydroQuebec for a scholarship.

937

938 **7 References:**

- 939 Ammann, C. M., and E. R. Wahl (2007), The importance of the geophysical context in
 940 statistical evaluations of climate reconstruction procedures, *Climatic Change*, *85*, 71-
 941 88 doi: doi: 10.1007/s10584-007-9276-x.
- 942 Baillie, R. T., and S.-K. Chung (2002a), Modeling and forecasting from trend-
 943 stationary long memory models with applications to climatology, , *International*
 944 *Journal of Forecasting* *18*, 215–226.
- 945 Baillie, R. T., and S.-K. Chung (2002b), Modeling and forecasting from trend-
 946 stationary long memory models with applications to climatology, *International*
 947 *Journal of Forecasting*, *18*, 215–226.
- 948 Biagini, F., Y. Hu, B. Øksendal, and T. Zhang (2008), *Stochastic Calculus for Fractional*
 949 *Brownian Motion and Applications*, Springer-Verlag, London.
- 950 Blender, R., K. Fraedrich, and B. Hunt (2006), Millennial climate variability: GCM-
 951 simulation and Greenland ice cores, *Geophys. Res. Lett.*, , *33*, , L04710 doi:
 952 doi:10.1029/2005GL024919.
- 953 Bryson, R. A. (1997), The Paradigm of Climatology: An Essay, *Bull. Amer. Meteor. Soc.*
 954 , *78*, 450-456.
- 955 Dijkstra, H. (2013), *Nonlinear Climate Dynamics*, 357 pp., Cambridge University
 956 Press, Cambridge.
- 957 Doblas-Reyes, F. J., I. Andreu-Burillo, Y. Chikamoto, J. Garcia-Serrano, V. Guemas, M.
 958 Kimoto, T. Mochizuki, L. R. L. Rodrigues, and G. J. van Oldenborgh (2013), Initialized
 959 near-term regional climate change prediction, *Nature Comm.*, 1-9 doi: doi:
 960 10.1038/ncomms2704.
- 961 Frank, D. C., J. Esper, C. C. Raible, U. Buntgen, V. Trouet, B. Stocker, and F. Joos
 962 (2010), Ensemble reconstruction constraints on the global carbon cycle sensitivity
 963 to climate, *Nature*, *463* (28) doi: doi:10.1038/nature08769.
- 964 Franzke, C. (2012), Nonlinear trends, long-range dependence and climate noise
 965 properties of temperature, *J. of Climate*, *25*, 4172-4183 doi: 10.1175/JCLI-D-11-
 966 00293.1.

- 967 Garcia-Serrano, J., and F. J. Doblas-Reyes (2012), On the assessment of near-surface
968 global temperature and North Atlantic multi-decadal variability in the ENSEMBLES
969 decadal hindcast, *Clim. Dyn.*, *39*, 2025–2040 doi: DOI 10.1007/s00382-012-1413-1.
- 970 Gripenberg, G., and I. Norros (1996), On the Prediction of Fractional Brownian
971 Motion *J. Appl. Prob.*, *33*, 400-410.
- 972 Haar, A. (1910), Zur Theorie des orthogonalen Funktionensysteme, *Mathematische*
973 *Annalen*, *69*, 331-371.
- 974 Hasselmann, K. (1976), Stochastic Climate models, part I: Theory, *Tellus*, *28*, 473-
975 485.
- 976 Hirchoren, G. A., and C. E. D'attellis (1998), Estimation Of Fractal Signals, Using
977 Wavelets And Filter Banks, *IEEE Transactions On Signal Processing*, *46*(6), 1624-
978 1630.
- 979 Hirchoren, G. A., and D. S. Arantes (1998), Predictors For The Discrete Time
980 Fractional Gaussian Processes, in *Telecommunications Symposium, 1998. ITS '98*
981 *Proceedings. SBT/IEEE International*, edited, pp. p49-53, IEEE, Sao Paulo
- 982 Huang, S. (2004), Merging Information from Different Resources for New Insights
983 into Climate Change in the Past and Future, *Geophys.Res. Lett.*, *31*, L13205 doi: doi :
984 10.1029/2004 GL019781.
- 985 Huybers, P., and W. Curry (2006), Links between annual, Milankovitch and
986 continuum temperature variability, *Nature*, *441*, 329-332 doi:
987 10.1038/nature04745.
- 988 Kolesnikov, V. N., and A. S. Monin (1965), Spectra of meteorological field
989 fluctuations, *Izvestiya, Atmospheric and Oceanic Physics*, *1*, 653-669.
- 990 Kolmogorov, A. N. (1940), Wiener'sche spiralen und einige andere interessante
991 kurven in Hilbert'schen Raum, *Doklady Akademii Nauk S.S.S.R.*, *26*, 115-118.
- 992 Koscielny-Bunde, E., A. Bunde, S. Havlin, H. E. Roman, Y. Goldreich, and H. J.
993 Schellnhuber (1998), Indication of a universal persistence law governing
994 atmospheric variability, *Phys. Rev. Lett.*, *81*, 729-732.
- 995 Laepple, T., S. Jewson, and K. Coughlin (2008), Interannual temperature predictions
996 using the CMIP3 multi-model ensemble mean, *Geophys. Res. Lett.*, *35* doi: L10701,
997 doi:10.1029/2008GL033576, 2008.
- 998 Livina, V. N., G. Lohmann, M. Mudelsee, and T. M. Lenton (2013), Forecasting the
999 underlying potential governing the time series of a dynamical system *Physica A* *392*,
1000 3891–3902 doi: doi.org/10.1016/j.physa.2013.04.036.
- 1001 Lovejoy, S. (2013), What is climate?, *EOS*, *94*, (1), 1 January, p1-2.
- 1002 Lovejoy, S. (2014a), Return periods of global climate fluctuations and the pause,
1003 *Geophys. Res. Lett.*, *41*, 4704-4710 doi: doi: 10.1002/2014GL060478.

- 1004 Lovejoy, S. (2014b), Scaling fluctuation analysis and statistical hypothesis testing of
 1005 anthropogenic warming, *Climate Dynamics*, 42, 2339-2351 doi: 10.1007/s00382-
 1006 014-2128-2.
- 1007 Lovejoy, S. (2015a), How accurately do we know the temperature of the surface of
 1008 the earth?, *Geophys. Res. Lett.* , (submitted June).
- 1009 Lovejoy, S. (2015b), Using scaling for macroweather forecasting including the pause,
 1010 *Geophys. Res. Lett.*, 41, 4704-4710 doi: doi: 10.1002/2014GL060478.
- 1011 Lovejoy, S., and D. Schertzer (1986), Scale invariance in climatological temperatures
 1012 and the local spectral plateau, *Annales Geophysicae*, 4B, 401-410.
- 1013 Lovejoy, S., and D. Schertzer (2010), Towards a new synthesis for atmospheric
 1014 dynamics: space-time cascades, *Atmos. Res.*, 96, pp. 1-52 doi: doi:
 1015 10.1016/j.atmosres.2010.01.004.
- 1016 Lovejoy, S., and D. Schertzer (2012a), Haar wavelets, fluctuations and structure
 1017 functions: convenient choices for geophysics, *Nonlinear Proc. Geophys.* , 19, 1-14 doi:
 1018 10.5194/npg-19-1-2012.
- 1019 Lovejoy, S., and D. Schertzer (2012b), Low frequency weather and the emergence of
 1020 the Climate, in *Extreme Events and Natural Hazards: The Complexity Perspective*,
 1021 edited by A. S. Sharma, A. Bunde, D. N. Baker and V. P. Dimri, pp. 231-254, AGU
 1022 monographs.
- 1023 Lovejoy, S., and D. Schertzer (2013), *The Weather and Climate: Emergent Laws and*
 1024 *Multifractal Cascades*, 496 pp., Cambridge University Press, Cambridge.
- 1025 Lovejoy, S., and M. I. P. de Lima (2015), The joint space-time statistics of
 1026 macroweather precipitation and space-time factorization, *Chaos in press*.
- 1027 Lovejoy, S., D. Scherter, and D. Varon (2013a), How scaling fluctuation analyses
 1028 change our view of the climate and its models (Reply to R. Pielke sr.: Interactive
 1029 comment on "Do GCM's predict the climate... or macroweather?" by S. Lovejoy et al.),
 1030 *Earth Syst. Dynam. Discuss.*, 3, C1-C12.
- 1031 Lovejoy, S., D. Schertzer, and D. Varon (2013b), Do GCM's predict the climate.... or
 1032 macroweather?, *Earth Syst. Dynam.* , 4, 1-16 doi: 10.5194/esd-4-1-2013.
- 1033 Lovejoy, S., J. P. Muller, and J. P. Boisvert (2014), On Mars too, expect macroweather,
 1034 *Geophys. Res. Lett.*, doi: 10.1002/2014GL061861.
- 1035 Mandelbrot, B. B. (1974), Intermittent turbulence in self-similar cascades:
 1036 divergence of high moments and dimension of the carrier, *Journal of Fluid*
 1037 *Mechanics*, 62, 331-350.
- 1038 Mandelbrot, B. B., and J. W. Van Ness (1968), Fractional Brownian motions,
 1039 fractional noises and applications, *SIAM Review*, 10, 422-450.

- 1040 Moberg, A., D. M. Sonnechkin, K. Holmgren, N. M. Datsenko, and W. Karlén (2005),
 1041 Highly variable Northern Hemisphere temperatures reconstructed from low- and
 1042 high - resolution proxy data, *Nature*, 433(7026), 613-617.
- 1043 Newman, M. (2013), An Empirical Benchmark for Decadal Forecasts of Global
 1044 Surface Temperature Anomalies, *J. of Clim.* , 26, 5260-5269 doi: DOI: 10.1175/JCLI-
 1045 D-12-00590.1.
- 1046 Newman, M. P., P. D. Sardeshmukh, and J. S. Whitaker (2003), A study of subseasonal
 1047 predictability, *Mon. Wea. Rev.*, 131, 1715-1732.
- 1048 Novikov, E. A., and R. Stewart (1964), Intermittency of turbulence and spectrum of
 1049 fluctuations in energy-dissipation, *Izv. Akad. Nauk. SSSR. Ser. Geofiz.*, 3, 408-412.
- 1050 Nuzman, C. J., and H. V. Poor (2000), Linear estimation of self-similar processes via
 1051 Lamperti's transformation, *J. Appl. Probab.*, 37, 429-452.
- 1052 Panofsky, H. A., and I. Van der Hoven (1955), Spectra and cross-spectra of velocity
 1053 components in the mesometeorological range, *Quarterly J. of the Royal Meteorol. Soc.*,
 1054 81, 603.
- 1055 Papoulis, A. (1965), *Probability, Random Variables and Stochastic Processes*, Mc Graw
 1056 Hill, New York.
- 1057 Penland, C., and P. D. Sardeshmukh (1995), The optimal growth of tropical sea
 1058 surface temperature anomalies, *J. Climate*, 8, 1999-2024.
- 1059 Rypdal, K., L. Østvand, and M. Rypdal (2013), Long-range memory in Earth's surface
 1060 temperature on time scales from months to centuries, *JGR, Atmos.*, 118, 7046–7062
 1061 doi: doi:10.1002/jgrd.50399.
- 1062 Sardeshmukh, P. D., and P. Sura (2009), Reconciling non-gaussian climate statistics
 1063 with linear dynamics, *J. of Climate*, 22, 1193-1207.
- 1064 Schertzer, D., and S. Lovejoy (1987), Physical modeling and Analysis of Rain and
 1065 Clouds by Anisotropic Scaling of Multiplicative Processes, *Journal of Geophysical*
 1066 *Research*, 92, 9693-9714.
- 1067 Smith, D. M., S. Cusack, A. W. Colman, C. K. Folland, G. R. Harris, and J. M. Murphy
 1068 (2007), Improved Surface Temperature Prediction for the Coming Decade from a
 1069 Global Climate Model *Science*, 317, 796-799.
- 1070 Vallis, G. (2010), Mechanisms of climate variability from years to decades, in
 1071 *Stochastic Physics and Climate Modelling*, edited by P. W. T. Palmer, pp. 1-34,
 1072 Cambridge University Press, Cambridge.
- 1073 Van der Hoven, I. (1957), Power spectrum of horizontal wind speed in the frequency
 1074 range from 0.0007 to 900 cycles per hour, *Journal of Meteorology*, 14, 160-164.
- 1075 Yaglom, A. M. (1955), Coprrrelation theory of processes with random stationary nths
 1076 increments (Russian). English translation:, Amer. Math. Soc. Trans. Ser., 8, p87-141,
 1077 *Mat. Sb. N.S.*, 37, 141-196.

- 1078 Yaglom, A. M. (1966), The influence on the fluctuation in energy dissipation on the
1079 shape of turbulent characteristics in the inertial interval, *Sov. Phys. Dokl.*, 2, 26-30.
- 1080 Yuan, N., Z. Fu, and S. Liu (2014), Extracting climate memory using Fractional
1081 Integrated Statistical Model: A new perspective on climate prediction, *Nature*
1082 *Scientific Reports*, 4, Article number: 6577 doi: doi:10.1038/srep06577.
- 1083
- 1084
- 1085

1086

Tables:1087
1088
1089

Row		1 year	5 year anomalies	9 year anomalies
Temperature, Residues				
1	Pre-industrial Multiproxies (1500-1900) ^a	0.112	0.105	0.098
2	T_{nat} : Residues (1880-2013) (no lag with CO ₂): $T_{anth}(t) \propto \log_2 p_{CO_2}(t)$	0.109	0.077 ^b	0.070
3	$T_{nat,20}$: residues from 1900-2013, 20 yr lag with CO ₂ : $T_{anth,\Delta t}(t) \propto \log_2 p_{CO_2}(t - \Delta t)$	0.108		
4	Standard deviation of the linearly detrended series 1880-2013 (residues, from a linear regression with the date).	0.163		
Deterministic Forecasts (GCM's)				
5	Without data assimilation 1983 - 2004 [<i>Smith et al., 2007</i>]	0.132	0.106	0.090
6	With data assimilation ("DePresSys") 1983 -2004, [<i>Smith et al., 2007</i>]	0.105	0.066	0.046
7	CMIP3 simulations with bias and variance corrections 1983 -2004, [<i>Laeppe et al., 2008</i>]	0.106	0.059	0.044
8	GFDL CM2.1 (initialized yearly) cited in [<i>Newman, 2013</i>]	0.11		
9	CMIP5 multimodel ensemble [<i>Doblas-Reyes et al., 2013</i>] not initialized ^c		0.095	
10	CMIP5 multimodel ensemble [<i>Doblas-Reyes et al., 2013</i>] initialized		0.06	
Stochastic Forecasts				
11	LIM ^d ([<i>Newman, 2013</i>])	0.085	(0.128)	(0.155)
12	[<i>Baillie and Chung, 2002a</i>] ARFIMA ^e	0.132±0.023		
13	[<i>Baillie and Chung, 2002a</i>] AR(1) ^f forecast	0.156±0.068		
14	SLIMM (one parameter, Stochastic 1880-2013) ^g	0.093	0.071 (0.102)	0.067 (0.105)

1090 Table 1: A comparison of Root Mean Square (RMS) variances (data residues) and
1091 hindcast errors (deterministic and stochastic models) of global scale, annual temperatures.
1092 See also fig. 2. Note that the GCM hindcasts are all “optimistic” in the sense that they
1093 use the observed volcanic and solar forcings and these would not be available for a true
1094 forecast. In comparison, the stochastic models forecast the responses to these (unknown)
1095 future forcings.

1096

1097 ^a The average of the three multiproxies from [*Huang, 2004*], [*Moberg et al., 2005*], [*Ammann*
1098 *and Wahl, 2007*]. These analyses were discussed in [*Lovejoy, 2014b*].

1099 ^b The empirical 5 year and 9 year anomaly values are close to the theoretical values

1100 $0.109^{-0.2} = 0.079$ and $0.109 9^{-0.2} = 0.070$.

1101 ^c The results here are for a subset of the CMIP5 simulations that were run with and without
1102 annual data assimilation (initialization).

1103 ^d Linear Inverse Modelling using, 20 eigenmodes, >100 parameters. The errors in brackets
1104 are for the temperatures, not anomalies. Note that the 9 year LIM value is almost identical
1105 to the standard deviation of the residues of the linear regression (fourth row of the table).

1106 ^e ARFIMA= Autogressive Fractionally Integrated Moving Average process; this is close to the
1107 SLIMM model used here. However the data and the data treatment were somewhat different. The
1108 annually, globally averaged temperatures from 1880 with a linear trend removed were used to
1109 make hindcasts over horizons of one to 10 years for the decades 1930, 1940, 1950, 1960. For
1110 each decade all the forecast errors were averaged. The value indicated here is the mean of the

1111 decade to decade mean error and the standard deviation of that error, the errors cannot therefore
1112 be directly compared with the others. The data were from a series compiled in 1986.

1113 ^f AR(1)= AutoRegressive order 1, is equivalent to “enhanced persistence” in the preceding. The
1114 variance reduction when using ARFIMA instead of AR(1) is 29%,

1115 ^g The values in parentheses are for 1 year resolution temperatures.

1116

1117

1118

Resolution		$\lambda_{2XCO_2,eff}$ (K/doubling, no lag, 1880- 2013)	$\lambda_{2XCO_2,eff}$ (K/doubling, no lag, 1880- 1998)	$\lambda_{2XCO_2,eff}$ (K/doubling, no lag, 1880- 1976)	$\lambda_{2XCO_2,eff}$ (K/doubling, 20 yr lag, 1900- 2013)
Monthly (dT _s)	Global	2.97±0.08	2.92±0.13	2.97±0.25	4.29±0.13
	Northern H.	3.41±0.11	3.11±0.17	3.10±0.33	4.99±0.18
Annual (LOTI)	Global	2.33±0.16	2.26±0.24	2.08±0.48	3.73±0.25
	Northern H.	2.56±0.23	2.25±0.34	2.41±0.65	3.96±0.38

1119 Table 2: The climate sensitivities estimated by linear regression of $\log_2 \rho_{CO_2}$ against the
1120 temperature anomalies at monthly and annual resolutions from global and northern
1121 hemisphere series. The far right column shows the 20 year lagged sensitivity to (1900-
1122 2013), i.e. using $T_{anth,\Delta t}(t) = \lambda_{2XCO_2,eff,\Delta t} \log_2(\rho_{CO_2}(t - \Delta t) / \rho_{CO_2,pre})$ where $\Delta t = 20$ years.

1123

1124

	Monthly	Annual	$H = \log(\sigma_{T,yr} / \sigma_{T,month}) / \log 12$
Global	0.201	0.109	-0.24
Northern Hemisphere	0.273	0.155	-0.23

1125 Table 3: The various standard deviations of the temperature residues (T_{nat}) after removing
1126 T_{anth} at monthly and annual resolution and the estimate of H obtained assuming perfect
1127 scaling over a factor of 12 in time scale, units, (K).

1128

1129

Resolution		$\langle E_T(\tau, \tau)^2 \rangle^{1/2}$	$\langle E_T(\tau, \tau)^2 \rangle^{1/2}$
		No lag	20 yr lag
Monthly	Global	0.148	0.146
	Northern H.	0.214	0.209
Annual	Global	0.093	0.092
	Northern H.	0.132	0.133

1130 Table 4: The hindcast standard deviations (in units of K) at the finest resolutions (1
1131 month, 1 year) for natural variability temperatures obtained from the unlagged and 20
1132 year lagged climate sensitivities. Note that the lag makes very little difference to the
1133 hindcast error variance.

1134

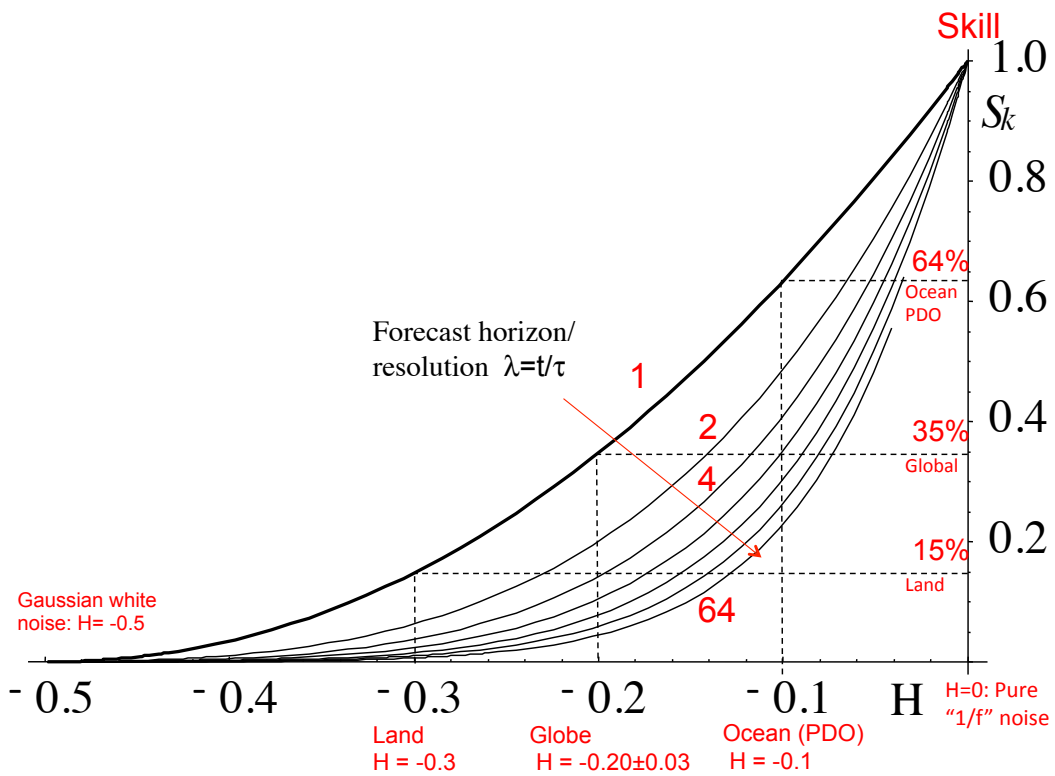
1135 **Figures**

1136

1137

1138

1139



1140

1141 Fig. 1a: Forecast skill for nondimensional forecast horizons $\lambda = (\text{horizon}/\text{resolution}) = 1, 2,$ 1142 $4, 8, \dots, 64$ (left to right) as functions of H . For reference, the rough empirical values for

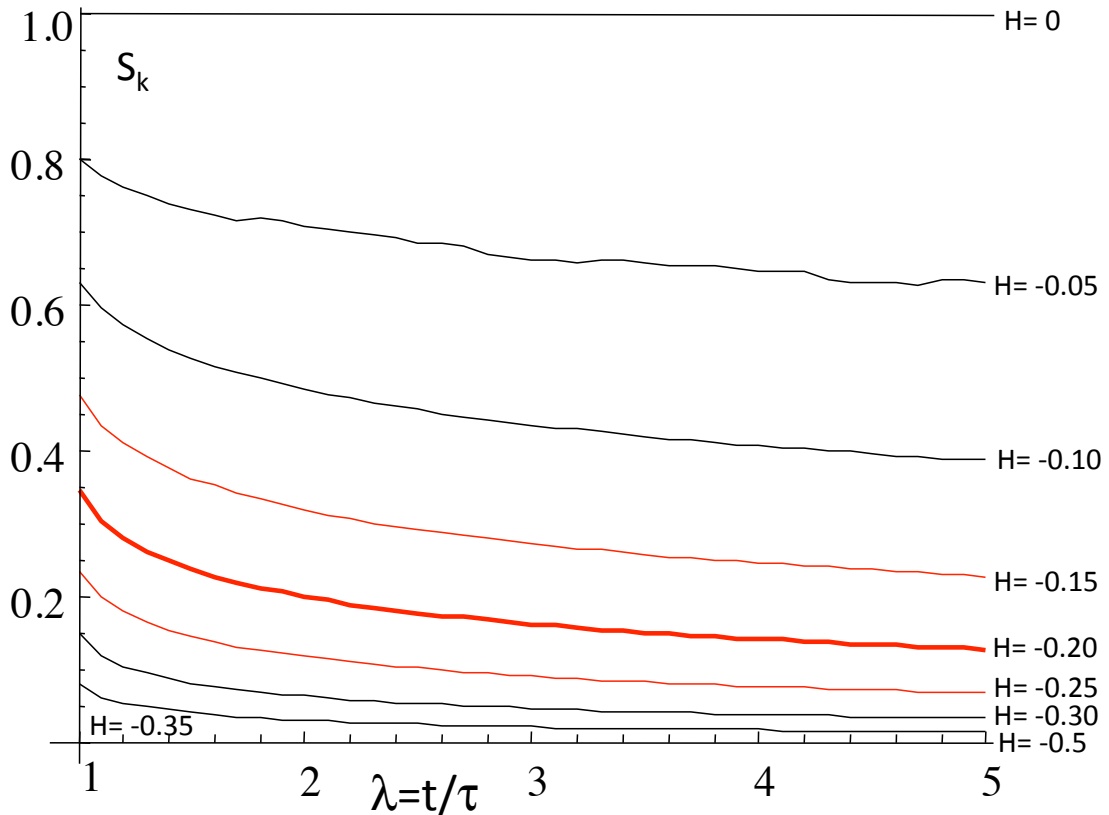
1143 land, ocean and the entire globe (the value used here, see below) are indicated by dashed

1144 vertical lines. The horizontal lines show the fraction of the variance explained (the skill,

1145 S_k , eq. 47) in the case of a forecast of resolution τ data at a forecast horizon $t = \tau$ ($\lambda = 1$;

1146 corresponding to forecasting the anomaly fluctuation one time unit ahead).

1147



1148

1149 Fig. 1b: The theoretical skill with infinite memory for various ratios of nondimensional

1150 forecast horizons λ over the range $0 > H > -0.35$ (top to bottom in steps of 0.05). The

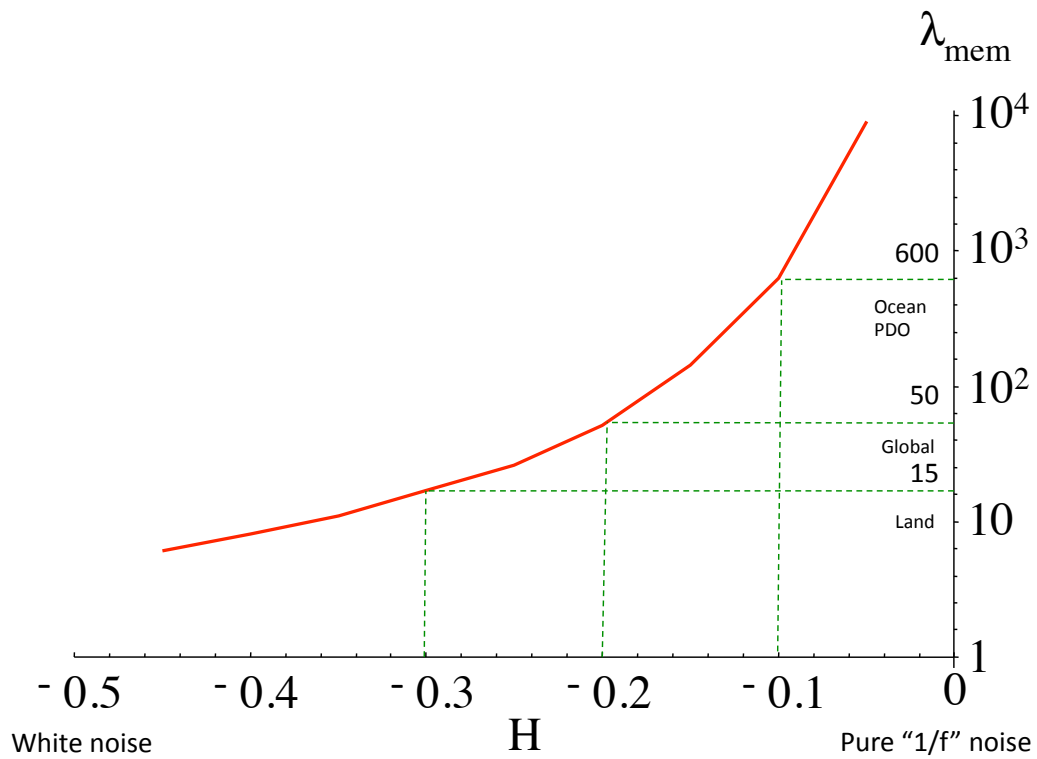
1151 limiting value $H = -1/2$ corresponds to Gaussian white noise with zero skill. The

1152 empirically relevant range for the whole earth ($H \approx -0.20 \pm 0.03$) is in red, thick the best

1153 estimated parameter ($H = -0.20$).

1154

1155



1156

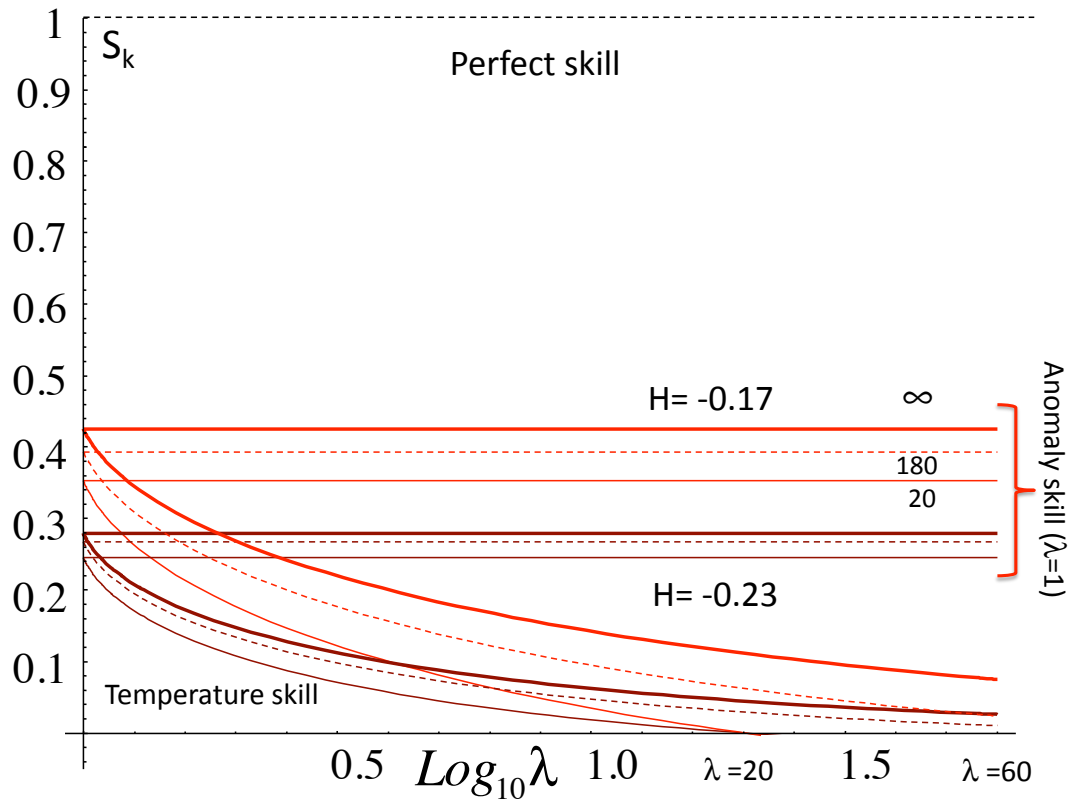
1157 Fig. 1c: This illustrates the potentially huge memory in the climate system (especially the

1158 ocean). It gives the λ_{mem} value such that $S_{x,\lambda_{mem}}(1)/S_{x,\infty}(1)=0.9$. When $H = -1/2$, there is

1159 no memory and λ_{mem} is not defined, it diverges when $H \rightarrow 0$.

1160

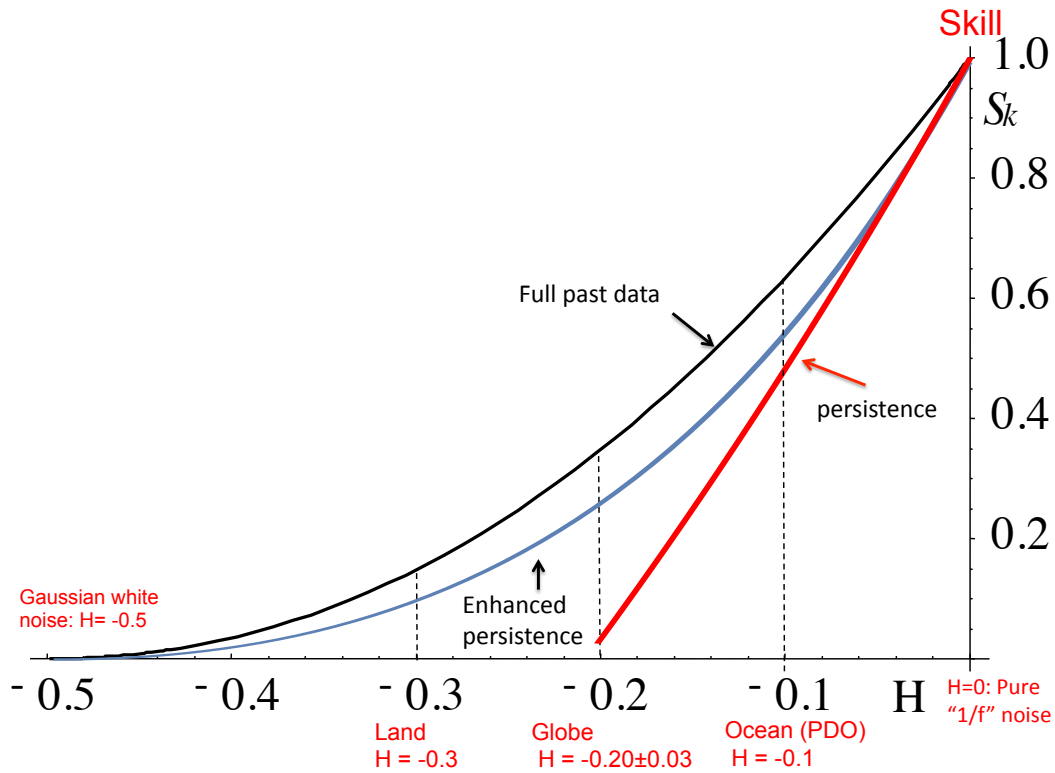
1161



1162

1163 Fig.1d: The theoretical skills for hindcasts with infinite (eq. 46) and finite memory (eq.
 1164 49) for the empirically relevant parameter range ($H = -0.23$, brown, bottom, $H = -0.17$,
 1165 red, top). The flat (constant skill) at the top are the curves for the anomaly forecasts (i.e.
 1166 with forecast horizon t is equal to the resolution τ so that $\lambda = 1$), the bottom curves are for
 1167 constant resolution τ with forecast horizon. In each case a triplet of curves is shown
 1168 corresponding to varying lengths of memories used in the forecast: infinite, 180 and 20
 1169 (the latter two corresponding to the those used for the monthly and global forecasts
 1170 analysed here).

1171

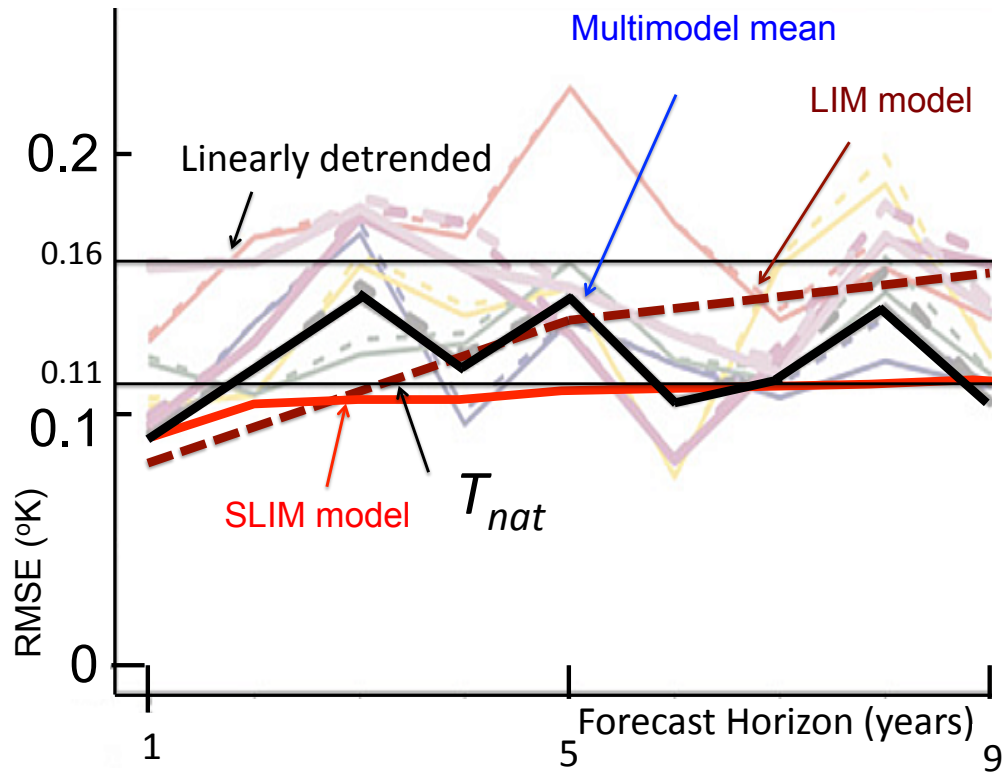


1172

1173 Fig. 1e: The skill of $\lambda = t/\tau = 1$ forecasts using the full memory (black, eq. 46, from fig.1174 1a), the corresponding classical persistence forecast (red), $S_k = 1 - 4(1 - 2^{2H})$ and the1175 corresponding "enhanced persistence" result (blue; for this $\lambda=1$ case, this is the same as1176 the AR(1) model forecast) with $S_k = (2^{2H+1} - 1)^2$. With classical persistence the skill1177 becomes negative for $H < \approx -0.2$, so it is not shown over the whole range.

1178

1179

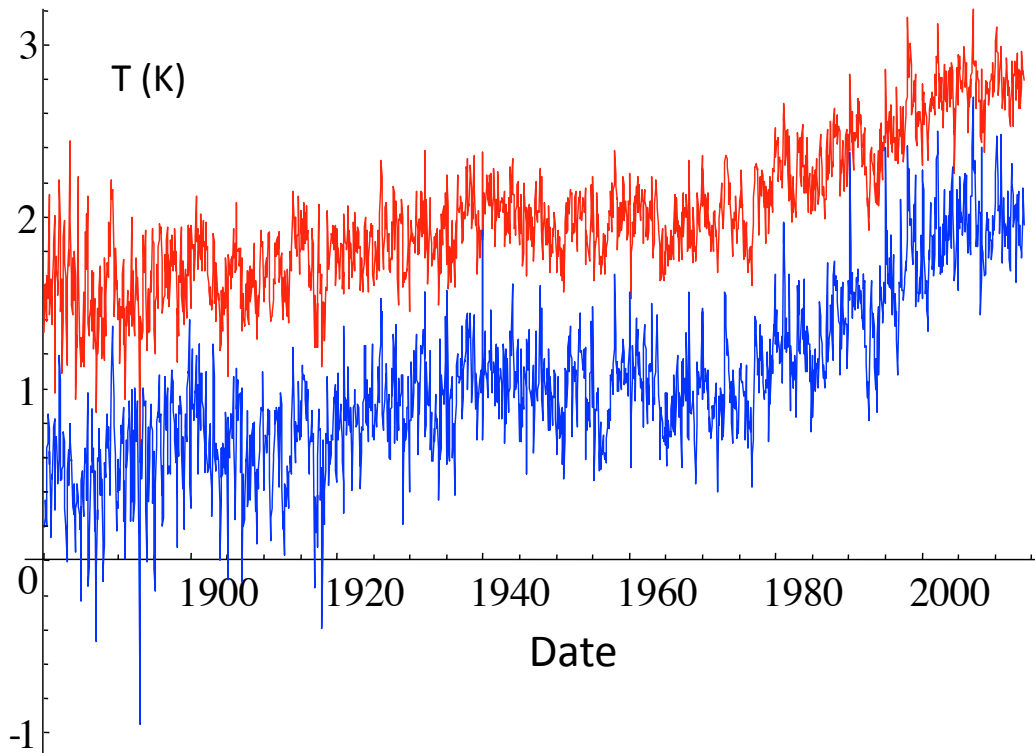


1180

1181 Fig. 2: ENSEMBLES experiment, LIM and SLIM hindcasts for global annual
 1182 temperatures for horizons 1 to 9 years. The light lines are from individual members of
 1183 the ENSEMBLE experiment, the heavy line is the multimodel ensemble adapted from
 1184 fig. 4 in [Garcia-Serrano and Doblas-Reyes, 2012]. This shows the RMSE
 1185 comparisons for the global mean surface temperatures compared to NCEP/NCAR (2 m
 1186 air temperatures). Horizontal reference lines indicate the standard deviations of T_{nat}
 1187 (bottom), and of the linearly detrended temperatures (top). Also shown are the RMS
 1188 error for the LIM model (from table 1, [Newman, 2013]) and the SLIMM.

1189

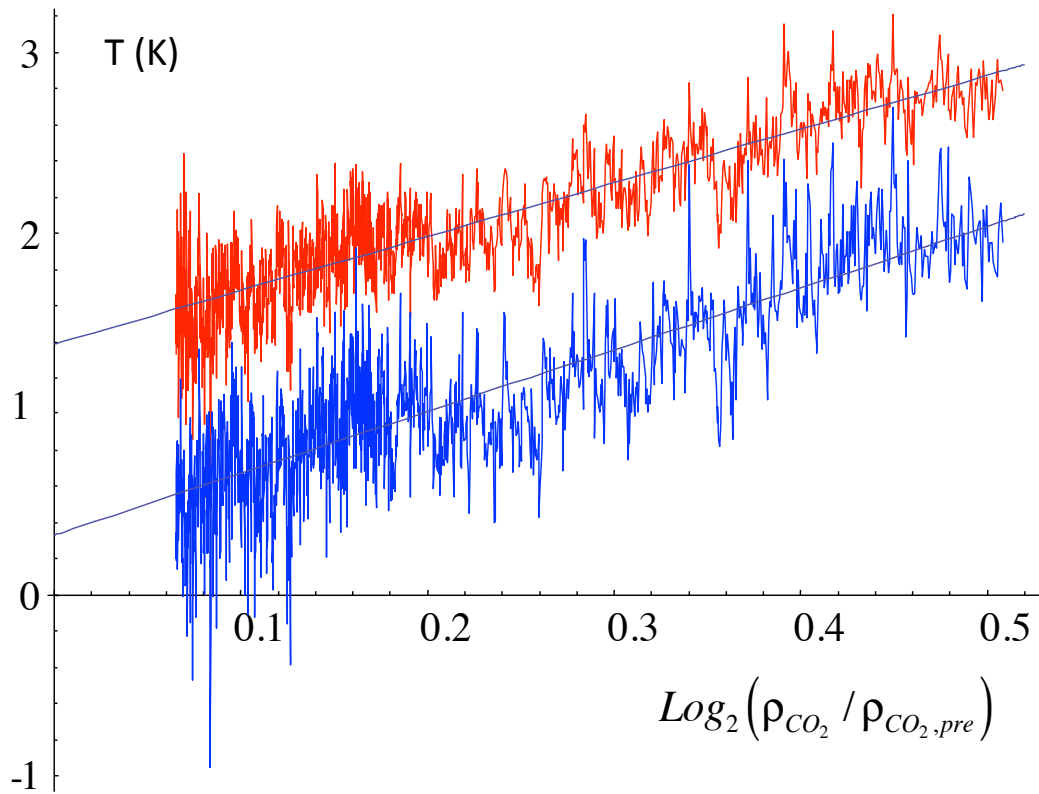
1190



1191

1192 Fig. 3a: The monthly surface temperature anomaly series from NASA GISS data (the
1193 monthly dTs series). Top (red) is the global average, displaced upward by 2 K for clarity,
1194 the bottom (blue) is the northern hemisphere series displaced upward by 1 K.

1195

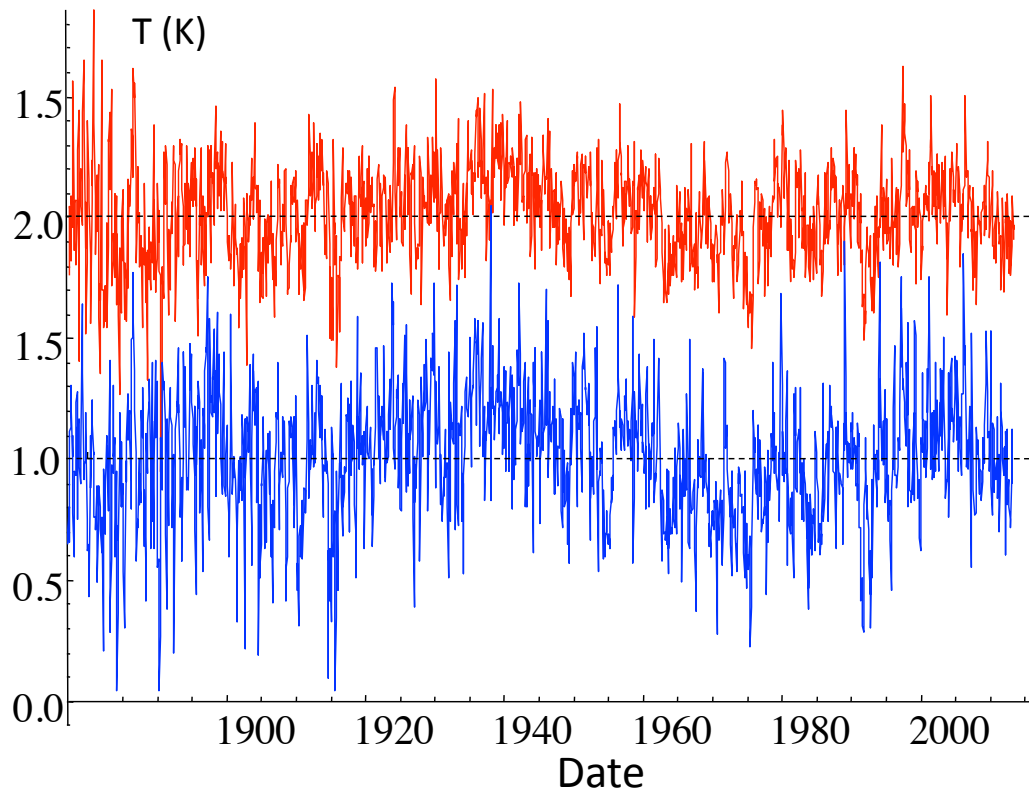


1196

1197 Fig. 3b: The same as fig. 3a but for the temperatures as functions of the logarithm of the
 1198 CO₂ concentration ρ_{CO_2} normalized by the preindustrial value $\rho_{CO_2,pre} = 277\text{ppm}$ (global
 1199 values are displaced upward by 2 K, northern hemisphere by 1 K for clarity). The
 1200 regressions have slopes indicated in table 2, they are the effective climate sensitivities to
 1201 CO₂ doubling.

1202

1203

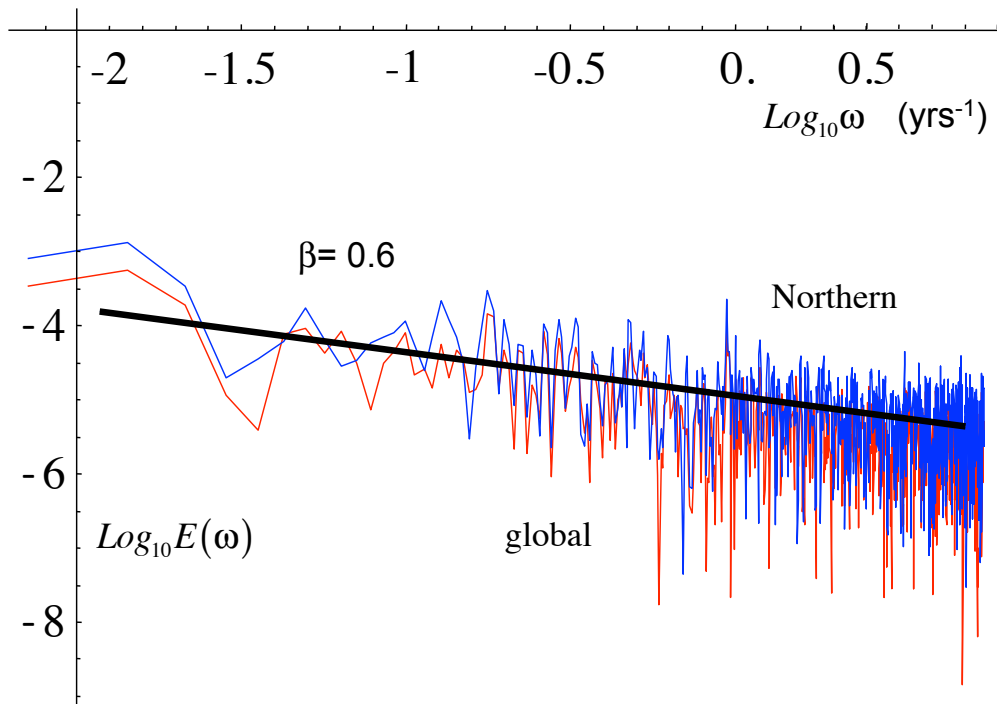


1204

1205 Fig. 3c: The residues of the linear regressions of fig. 3b; the estimate of the natural
1206 variability, again the global (red, top), northern hemisphere (blue, bottom) have been
1207 shifted upward by 1 K for clarity.

1208

1209

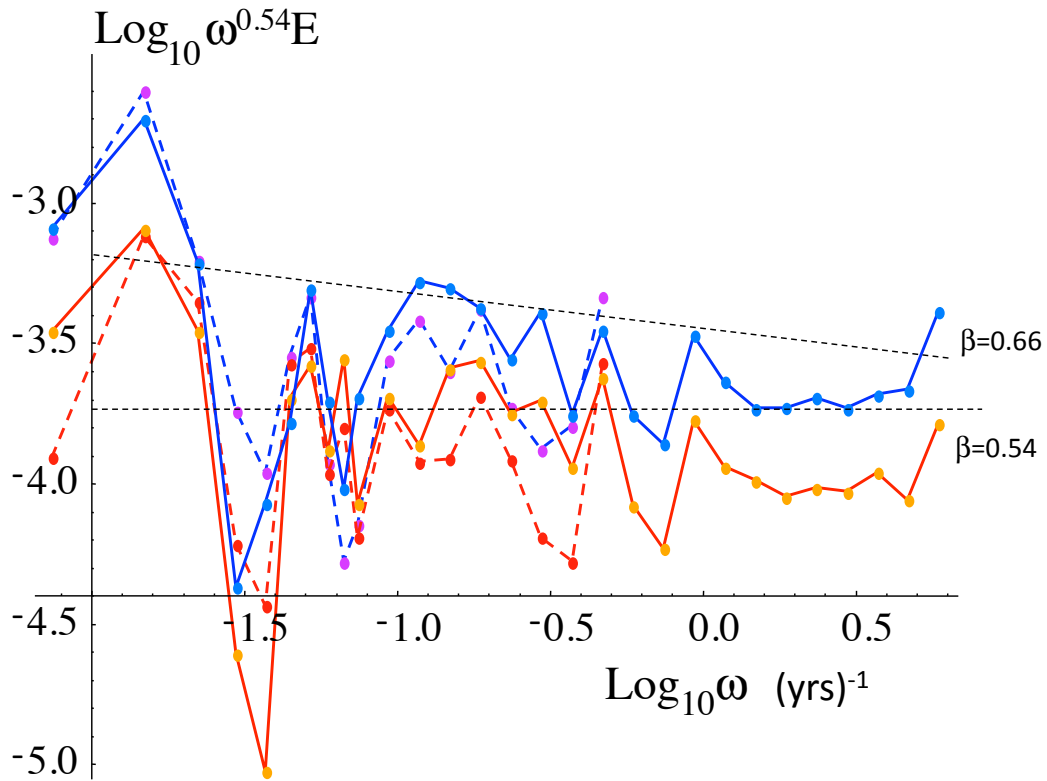


1210

1211

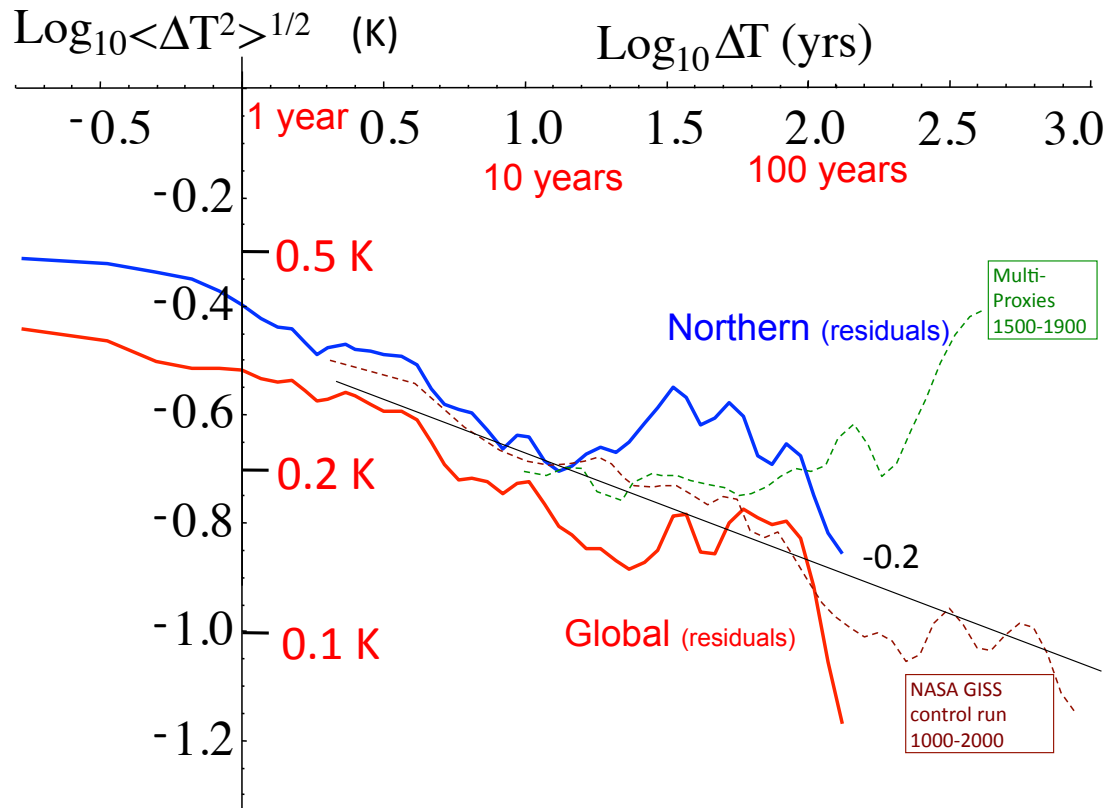
1212 Fig. 4a: The spectrum of the monthly residues for northern (blue) and global (red) data.

1213 The slope $\beta = 0.6$ is shown corresponding to the best overall estimate ($H = -0.20$).



1214

1215 Fig. 4b: The northern hemisphere (top, blue) and global (bottom, red) spectra, at monthly
 1216 (solid) and annual (dashed) resolutions using the NASA GISS surface temperature
 1217 anomaly series from 1880-2013. For frequencies higher than the lowest factor of ten,
 1218 averages have been made over ten frequency bins per order of magnitude in scale. In
 1219 addition, the spectra have been “compensated” by multiplying by $\omega^{0.54}$ so that spectra
 1220 with $H = -0.23$ ($\beta = 0.54$) appear flat. The range $-0.17 < H < -0.23$ corresponding to one
 1221 standard deviation limits ($\beta = 1 + 2H$, i.e. ignoring small multifractal intermittency
 1222 corrections) corresponds to $0.54 < \beta < 0.66$, the lower and upper bounding reference lines
 1223 are shown as dashed.

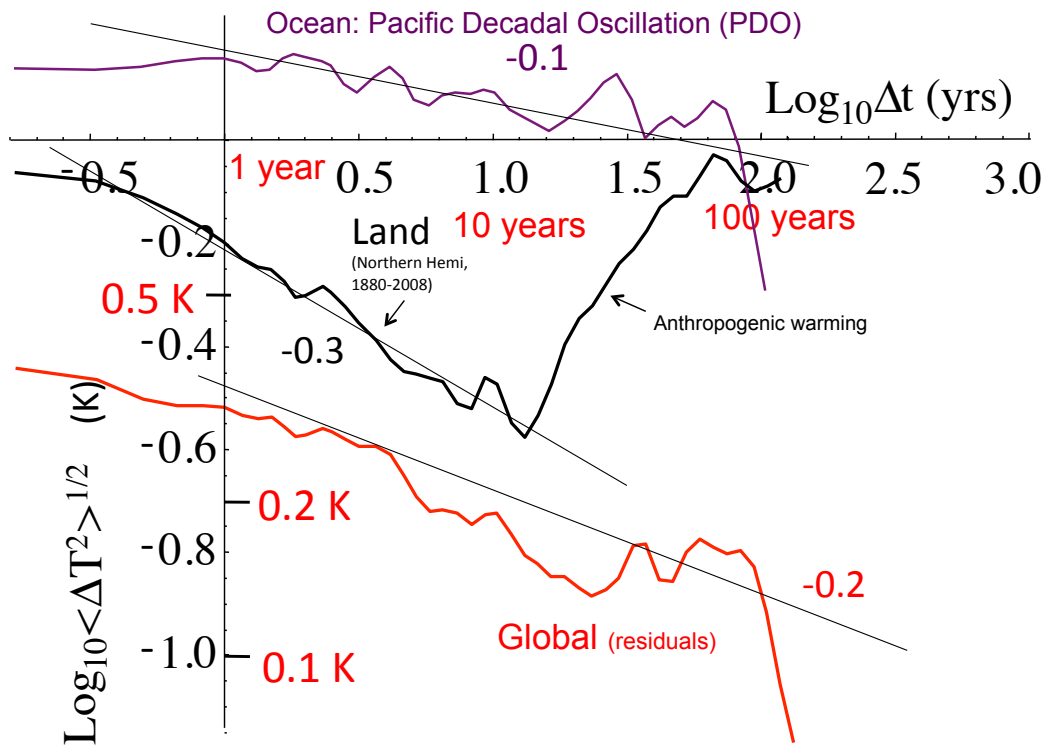


1224

1225 Fig. 4c: The RMS Haar fluctuations for the northern (blue) and global (red) monthly
 1226 series. Reference lines with slopes $H = -0.2$ are shown, we see that the scaling is fairly
 1227 well respected up to ≈ 100 years. The raw Haar fluctuations have been multiplied by 2
 1228 (the “canonical calibration”, see [Lovejoy and Schertzer, 2012a]) in order to bring
 1229 them closer to the anomaly fluctuations. Also shown is the NASA control run and the
 1230 pre-industrial multiproxies. They all agree quantitatively very well up to about 100 years
 1231 where the pre-industrial natural climate change starts to become important. This shows
 1232 that the monthly scale residuals are almost exactly as simulated by the GISS model

1233 without any anthropogenic effects, supporting the idea that T_{nat} is a good estimate of the
 1234 natural variability.

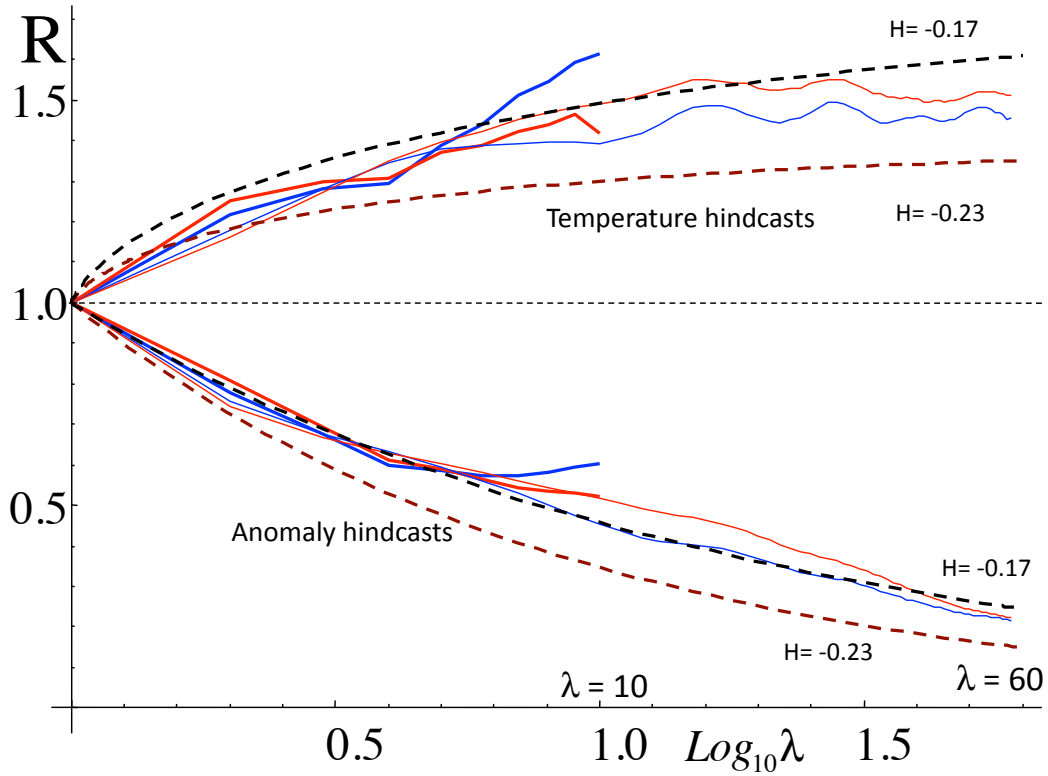
1235



1236

1237 Fig. 4d: Comparisons of the RMS Haar fluctuations of global scale natural variability
 1238 (T_{nat}) from fig. 4c, with those from land only (HADCRUT3, black) and from the Pacific
 1239 Decadal Oscillation (PDO, top, purple, from [Lovejoy and Schertzer, 2013], fig.
 1240 10.14). Reference lines of slopes $H = -0.1, -0.2, -0.3$ are shown close to the curves for
 1241 ocean, globe and land respectively.

1242



1243

1244

1245 Fig. 5: The dimensionless ratios (R) of the hindcast error variances to the variance at the
 1246 smallest resolution and horizon t equal to the resolution τ for both temperature (with

1247 horizon $\lambda\tau$, resolution τ (top, $R = \langle E_T(\lambda\tau, \tau)^2 \rangle / \langle E_T(\tau, \tau)^2 \rangle = 1 + (2 + 2H)F_H(\lambda)$) and

1248 anomaly, with horizon $\lambda\tau$, resolution $\lambda\tau$ (bottom, $R = \langle E_T(\lambda\tau, \lambda\tau)^2 \rangle / \langle E_T(\tau, \tau)^2 \rangle = \lambda^{2H}$).

1249 The red are global, the blue northern hemisphere, the thick, shorter curves are at annual
 1250 resolution ($\tau=1$ yr) and the thin, longer lines are at monthly resolution ($\tau=1$ month).

1251 Also shown (dashed) are the theory curves for $H = -0.17, -0.23$ (top (black) and bottom

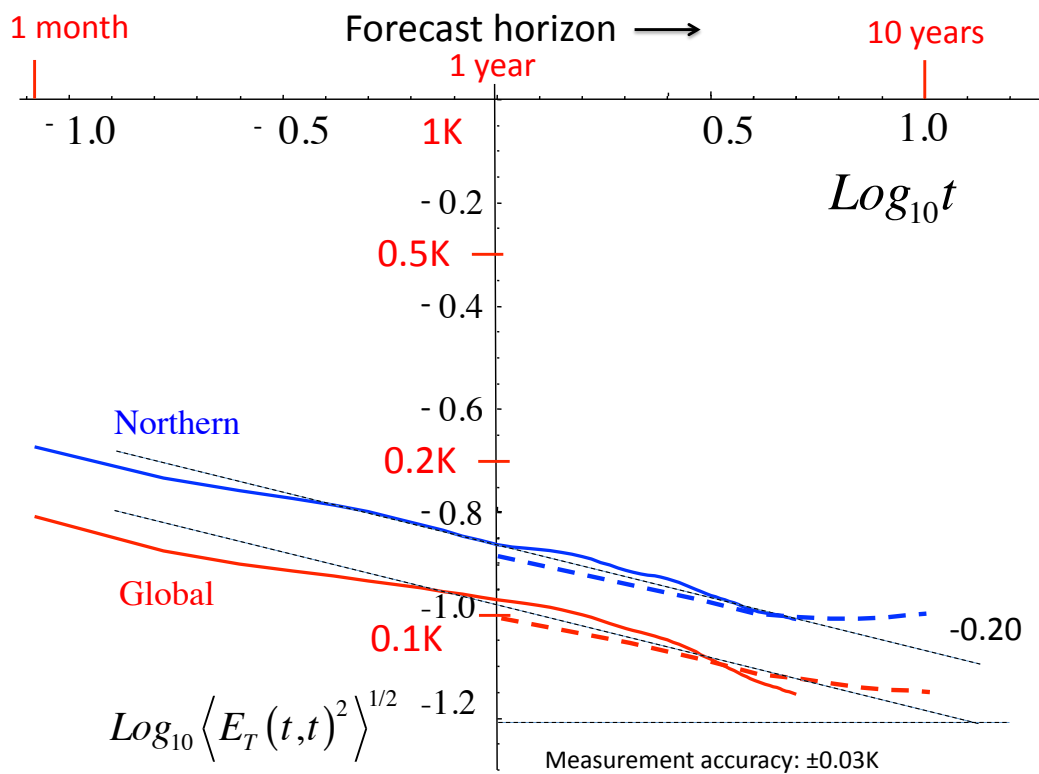
1252 (brown) of each dashed pair respectively). The data closely follow the $H = -0.17$ curves.

1253 The standard deviations at the highest resolution $\langle E_T(\tau, \tau)^2 \rangle^{1/2}$ are given in table 4. This
 1254 plot has no adjustable parameters.

1255

1256

1257



1258

1259 Fig. 6: A log-log plot of the standard deviations of the anomaly hindcasts with the
 1260 theoretical reference line corresponding to $H = -0.20$. The solid lines are for the monthly
 1261 data, the dashed lines for annual data, red for global, blue for northern hemisphere.

1262

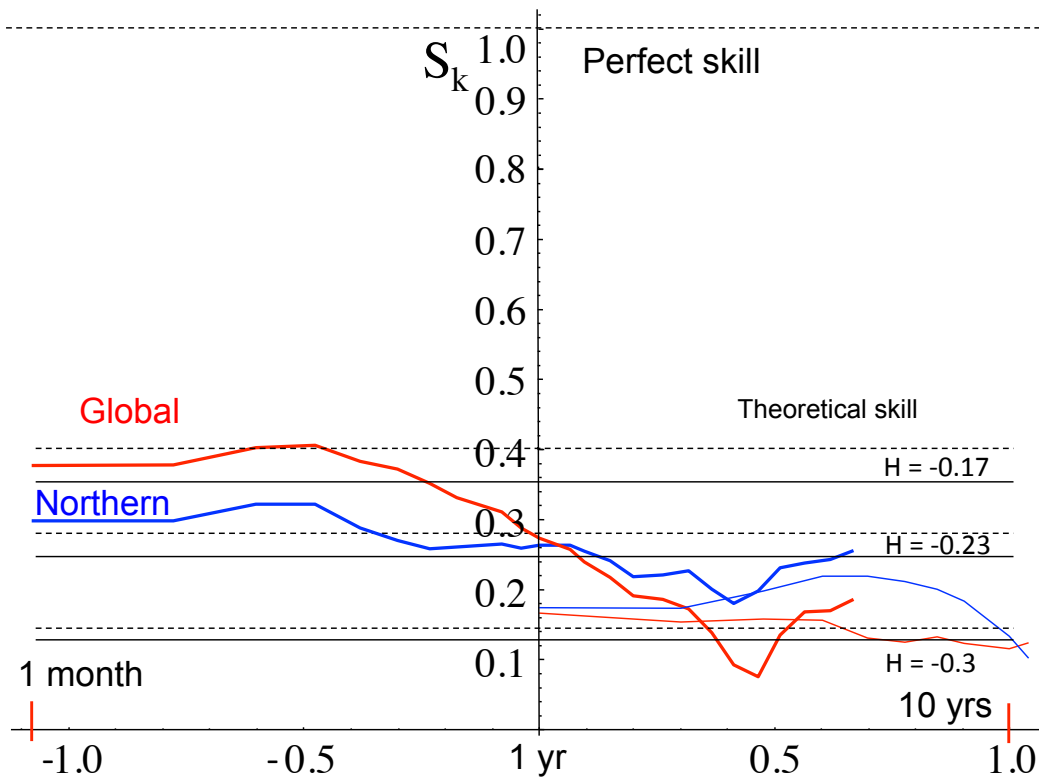
1263

1264

1265

1266

1267



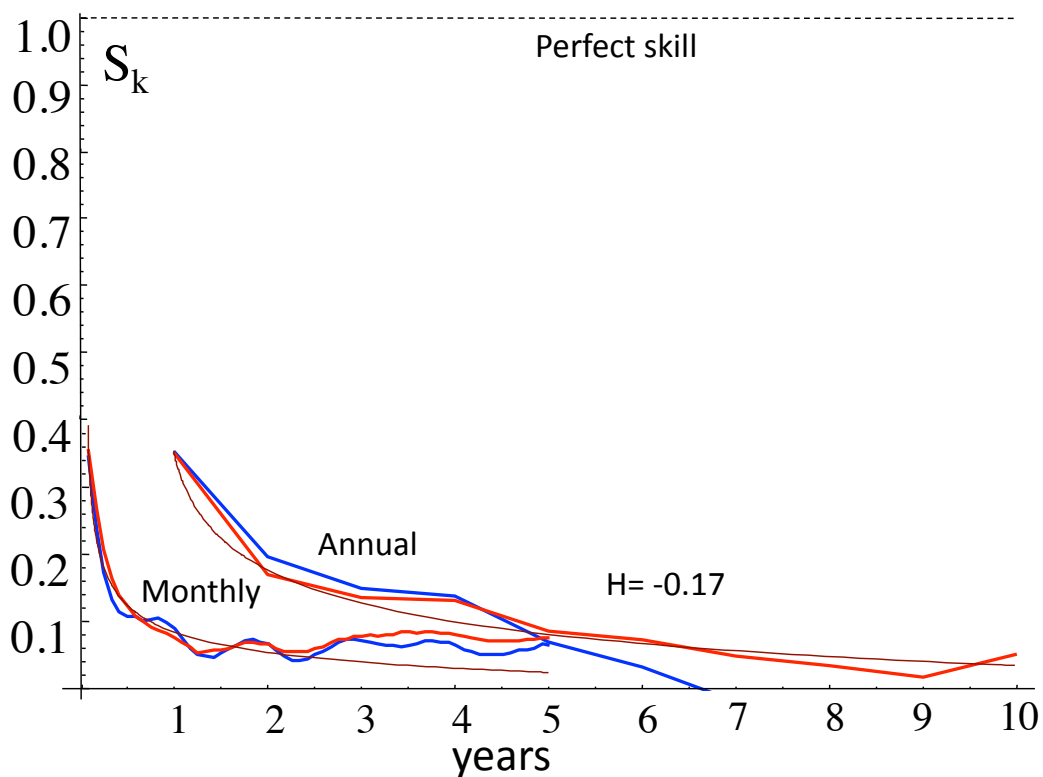
1268

1269

1270 Fig. 7: The anomaly forecast skill on a log-linear plot for both all series (annual thin,
 1271 monthly thick, global red, northern hemisphere (blue). Also shown are pairs of

1272 theoretical predictions (constant skill independent of the forecast horizon) for various
 1273 values of H , the top (dashed) member of the pair is for an infinite memory, the bottom
 1274 solid line is for the finite memory used here: (the monthly series has a memory of 180,
 1275 the annual series has 20). This plot has no adjustable parameters.

1276

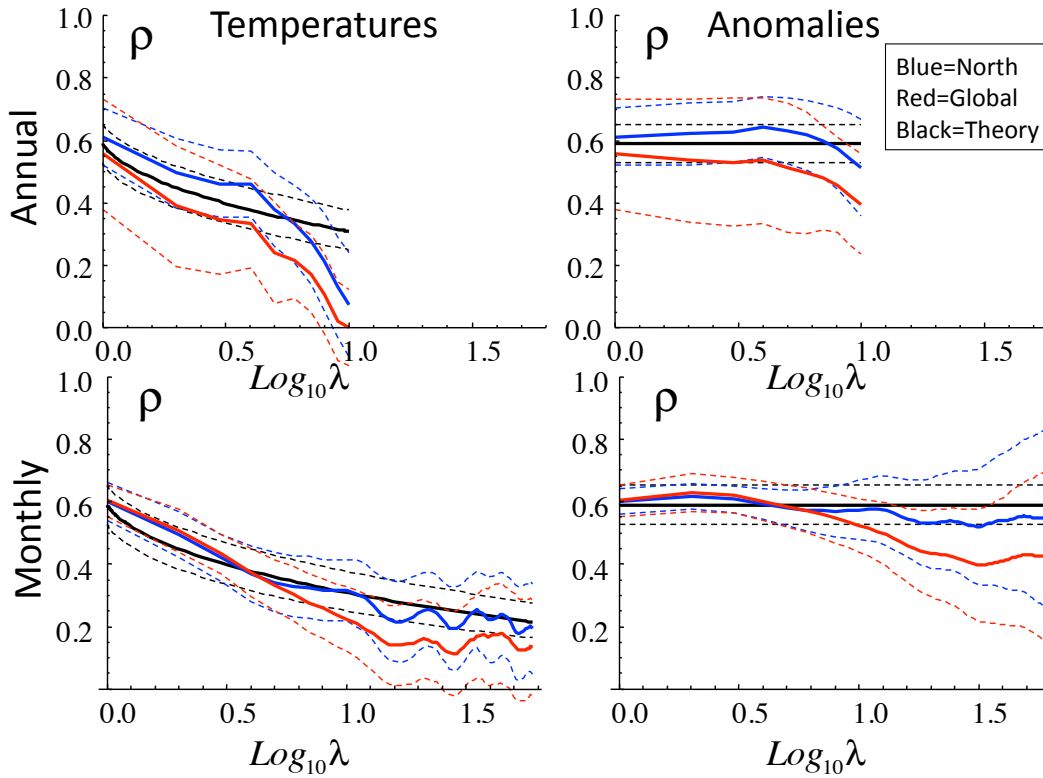


1277

1278 Fig. 8: The forecast skill for the temperature at fixed resolutions (one month, bottom left,
 1279 one year, upper right) for global (red) and northern hemisphere (blue) series. Also shown
 1280 are the exact theoretical curves (for $H = -0.17$) that take into account the finite memories
 1281 of the forecasts (20 years, 15 years annual, monthly series respectively). The raw curves
 1282 were shifted a little upward so that their long-time parts were close to the theory; this is

1283 equivalent to using the theory to improve the estimate of the ensemble average skill from
 1284 the single series that were available.

1285



1286

1287 Fig. 9: The empirical correlations of the forecast temperatures (left column) and
 1288 anomalies (right column), the same data as previous but with different empirical
 1289 comparisons and also with comparisons with theory for $H = -0.2$ (thick black), $H = -0.17$,
 1290 -0.23 top and bottom dashed black. Now note that in all cases the one standard deviation
 1291 bounds (dashed) on the empirical and theoretical curves overlap virtually throughout.
 1292 The theory curves have no adjustable parameters.

